FOI-R--0344--SE
November 2001
ISSN 1650-1942

FOI
SWEDISH DEFENCE
RESEARCH AGENCY

Scientific Report

Lars Sjöqvist, Sverker Hård, Stephane Junique, Bertrand Noharet and Per Rudquist

Retroreflective Free-space Optical Communication

System analysis and performance

Sensor Technology
SE-581 11 LINKÖPING

Swedish Defence Research Agency, FOI
Division of Sensor Technology
P.O. Box 1165
SE-581 11 Linköping

FOI-R--0344--SE
November 2001

Scientific Report

Lars Sjöqvist, Sverker Hård, Stephane Junique, Bertrand Noharet and Per Rudquist

Retroreflective Free-space Optical Communication

System analysis and performance

Issuing organization
Swedish Defence Research Agency, FOI
Division of Sensor Technology
P.O. Box 1165
SE-581 11 Linköping

Report number, ISRN
FOI-R--0344--SE

Report type
Scientific Report

Forskningsområde
4. C4ISR

Month, Year
November 2001

Project no.
E3831

Customers code
5. Commisioned research

Sub area code
41 C4I

Authors/s (editor/s)
Lars Sjöqvist, Sverker Hård, Stephane Junique, Bertrand Noharet and Per Rudquist

Project manager
Lars Sjöqvist

Approved by
Svante Ödman

Scientifically and technically responsible
Lars Sjöqvist

Report title (In translation)
Retroreflective Free-space Optical Communication. System and Performance Analysis

Abstract (not more than 200 words)
Free-space optical communication shows several interesting features for military applications such as transfer of large data quantities, covert data transfer, low jamming risk and overhearing, small volume and low weight etc. In retroreflective free-space optical communication a passive receiver is used to intensity modulate light and transfer data to a transceiver unit. The transceiver unit can be implemented with a non-mechanical beam steering feature for link establishment, tracking and signal optimisation. The retromodulating receiver can use multiple quantum well modulators to optically modulate the intensity of the light.

This report describes a system analysis of a retromodulating free-space optical communication system using MQW modulators for the retroreflecting receiver and non-mechanical beam steering using liquid crystal spatial light modulators. Different system designs and technics are reviewed and discussed. Performance calculations including effects from atmospheric attenuation, turbulence and diffraction have been carried out. Problems related to the atmospheric effects and different designs of the retroreflecting receiver are emphasised.

Keywords
Optical communication, MQW, retroreflective, modulator, beam steering, SLM

Further bibliographic information

Language
English

ISNN 1650-1942

Pages 69

Utgivare
Totalförsvarets Forskningsinstitut, FOI
Avdelningen för Sensorteknik
Box 1165
SE-581 11 Linköping

Rapportnummer, ISRN
FOI-R--0344--SE

Klassificering
Scientific Report

Forskningsområde
4. Spaning och ledning

Månad, år
November 2001

Projektnummer
E3831

Verksamhetsgren
5. Uppdragsforskning

Delområde
41 Ledning med samband, telekom och IT-system

Författare/redaktör
Lars Sjöqvist, Sverker Hård, Stephane Junique, Bertrand Noharet and Per Rudquist

Projektledare
Lars Sjöqvist

Godkänd av
Svante Ödman

Teknisk och/eller vetenskapligt ansvarig
Lars Sjöqvist

Rapportens titel
Retroreflektiv fri optisk kommunikation. System och prestandastudie.

Sammanfattning (högst 200 ord)
Fri optisk kommunikation har flera intressanta egenskaper för militära tillämpningar som möjlighet till överföring av stora datamängder, smygande kommunikation, låg störningsrisk och överhörning, lätta och kompakta system etc. I ett retroreflekterande optiskt kommunikationssystem används en passiv mottagare (retromodulator) för att modulera intensiteten hos reflekterat ljus och överföra data till en mottagarenhet. Mottagarenheten kan användas med icke-mekaniskt laserstrålstyrning för länketablering, målföljning och signaloptimering. Retromodulatorn kan bestå av kvantbrunnsmodulatorer (MQW) för att modulera det reflekterade ljuset.

Den här rapporten beskriver en systemanalys och prestandastudie för ett optiskt kommunikationssystem där MQW-modulatorer används i en retromottagare och icke-mekanisk strålstyrning åstadkommes med vätskekristall SLM:er (spatiella ljusmodulatorer). Systemaspekter och olika tekniker har diskuterats och sammanfattats. Prestandaberäkningar inkluderar effekter från atmosfärdämpning, turbulens och diffraktion. Problem relaterade till atmosfäriska effekter och olika utformningar av retromottagaren belyses.

Nyckelord
Optisk kommunikation, MQW, retroreflektion, modulator, strålstyrning, SLM

Övriga bibliografiska uppgifter

Språk
Engelska

ISNN 1650-1942

Antal sidor: 69

Distribution enligt missiv

CONTENT

1 INTRODUCTION

Free-space optical communication possesses several attractive features for military applications[1]. The need for secure high speed data links in future mobile and stationary sensor system makes free-space optical communication an interesting alternative to more conventional methods. Traditional free-space optical communication systems designed for space applications, such as satellite communication, is complex and expensive. During the recent years research has been focused on developing less complex systems for ground-to-ground scenarios. Retroreflective free-space optical communication provides a new concept for optical communication where a passive receiver is employed. Basically, the retromodulating receiver consists of an electro-optic (EO) modulator and corner cube retroreflector. The corner cube reflects incident light in the same direction as it arrived and the modulator adds an intensity modulation if "on-off" keying is used as modulation scheme. The data transfer rate from the retromodulating receiver is limited by the speed of the EO-modulator. A transceiver, consisting of an interrogating continuous wave (cw) laser and an optical receiver channel, are used to extract modulated information from the retromodulating receiver (figure 1).

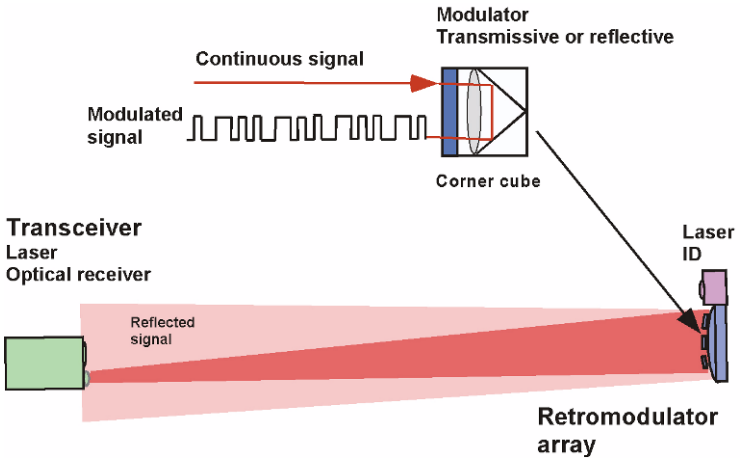

Figure 1. Principle of retroreflective free-space optical communication.

The retromodulating array has no active components making it simple in technical design. The receiver can be realised by utilising several single element retromodulators in parallel to increase the effective aperture area and the field of view. Retroreflective optical communication has several attractive features for military applications. By reducing the technical complexity of the receiver in a free-space communication system the weight, volume and power dissipation can be significantly decreased. One critical component is the electro-optical modulator transforming the information into intensity modulated reflected light. Modulators based on multiple quantum wells (MQW's) and liquid crystals (LC) have been used in retroreflective communication experiments[2],[3],[4],[5],[6]. MQW modulators have the advantage of providing a fast temporal response allowing data transfer rates of the order 10 Mbit/s and modulators with large apertures (~1 cm^2)[2]. Liquid crystal optical modulators have also been investigated for communication purposes[6]. Due to the slower temporal response LC modulator (three orders in magnitude lower than MQW's) are not suitable for high speed data transfer applications.

Spatial light modulators (SLM's) provide new methods to steer a laser beam and perform beam shaping[7]. Using two-dimensional (2D) phase patterns the wavefront of the beam is modulated and spatial features can be altered. One common way to accomplish beam steering is to utilise blazed phase gratings. Different technologies such as liquid crystals, micromechanical mirrors and multiple quantum wells have been investigated for a variety of SLM applications. Commercial liquid crystal SLM's (nematic and ferroelectric) are available for different photonics applications e.g. optical correlation, beam steering, beam shaping and adaptive optics. The parameters important for the performance of LC SLM's are pixel dimensions, array size, fill factor, response time and frame rate of the device. An analogue phase response, of at least one full optical wave at the design wavelength, should be possible to achieve to obtain efficient beam steering. Implementing an SLM for beam steering in a retromodulating communication system offers new capabilities for beam control. Important functions are link establishment, pointing and tracking. The performance of the optical transmitter is dependent on the SLM used for beam steering. System performance and critical parameters need to be defined and evaluated using LC SLM's for the beam control function in retromodulating communication.

Another important issue considering a retromodulating optical communication system is atmospheric effects[8]. Atmospheric aerosols, natural and artificial, give rise to scattering of the radiation and molecular absorption. These effects are weather dependent and result in a total attenuation of the beam intensity. The range performance is dependent on the atmospheric scattering and absorption. Turbulence effects, due to alterations in the refractive index of air, cause beam wandering, intensity variations (scintillations), angle-of-arrival fluctuations and beam broadening. Turbulence effects can also introduce signal fading and increase the bit-error probability. The direction of the communication channel, i.e. slant or horisontal path, affects the influence of the turbulence. In a horisontal communication path close to ground turbulence effects must be taken into account in studies of system performance. For a retromodulating free-space communication system double-passage effects are of specific interest.

Discussing the performance of a retromodulating optical communication system the overall features, sub-components and critical parameters need to be considered. The optical transceiver consist of the laser source, beam steering components, additional passive optics and the optical receiver channel including the detector. Noise and stray-light must be minimised to obtain the best performance. Optimal performance is obtained by carefully balancing crucial parameters in the transceiver and the retromodulator. Example of important issues from a system application point of view are: field of view, range performance, weather sensitivity, data transfer rates etc.

The objective of this report was to study performance and present a system analysis of a free-space optical communication system based on retromodulation. The system is assumed to use MQW technology for the retromodulating receiver and LC SLM's for non-mechanical beam steering. Models used to calculate performance and extract certian critical parameters have been developed. For example, the turbulence influence on a retromodulating optical communication link is considered in some detail. A numerical model based on physical optics and angular spectrum propagation was used to study the combined effects of diffraction and turbulence. Principles for link establishment, tracking and beam steering utilising optical phased array technology based on liquid crystal SLM's are discussed. The design and performance of AlGa/GaAs multiple quantum well

modulators were reviewed. Important parameters and design layouts of the transceiver (consisting of the laser transmitter and the optical receiver channel) and optical solutions for the retromodulating receiver were also considered.

2 MILITARY APPLICATIONS

In future battlefield scenarios the concept “information superiority” is believed to play an important role. The key for information advantage is efficient and secure communication channels. Free-space optical communication possess several interesting features making it interesting for military applications. In particular, retromodulating optical communication is of interest since it can provide technical solutions having low power consumption, small volume and low weight. Free-space optical communication also gives a secure communication alternative since the angular divergence of the laser beam is low preventing overhearing and making the link jam resistant. The potential for extremely high data transfer rates is another factor making optical communication important in future communication networks.

Several scenarios can be imagined where retromodulating optical communication systems play an important role in future military information transfer (Table 1). In ground-to-ground scenarios stationary retromodulators can be used in network configurations to transfer data to individual soldiers or fighting vehicles (figure 2a). Information transmitted between fighting vehicles may contain target information, sensor data such as e.g. images etc. The advantage of using retromodulating techniques in this scenario is the simplified receiver. By adapting the field of view of the receiver tracking solutions using gimbals in the transceiver end may be avoided. The ranges in the ground-to-ground scenario can be between 0.1 to 5 km. At these short ranges the laser beam divergence can be increased in order to reduce the required tracking precision of the transceiver. Another aspect is; if high data rate transfer is possible the time necessary for transmission can be reduced. One interesting aspect is to combine a free-space optical retroreflective communication system with other type of military laser systems such as laser countermeasures or laser radar for surveillance and target identification.

One required feature is the ability to transfer data during vehicle movement. The ground-to-ground scenario may also contain stationary retromodulating receivers where data can be extracted. If non-visible wavelengths are used for the communication channel the probability of discovery is low. Preferably, the wavelength should be shifted towards 1.55 μm or longer in order to reduce the risk of discovery and obtain an eye-safe channel. One limiting factor is the optical modulator since different technologies usually are wavelength dependent. MQW modulators using the material combination AlGaAs/GaAs operate at λ = 850 nm, which is not optimal from a tactical point of view. However, alternative material combinations are under development aiming to shift the wavelength further into the infrared region.

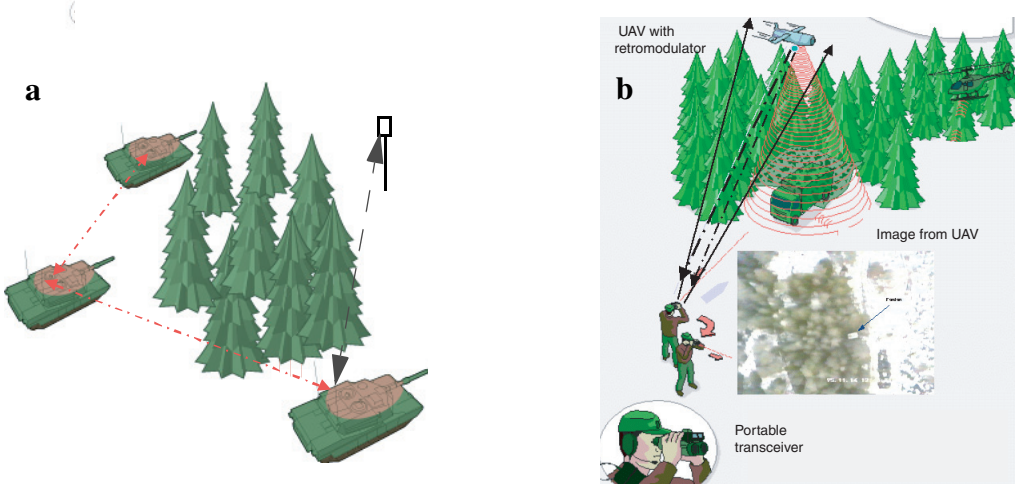

Figure 2. a) Example of ground-to-ground communication between tanks. b) Portable transceiver communicating with an UAV.

Simple and light-weight communication systems are also of interest for individual soldiers. A concept of a portable retromodulating communication application is depicted in figure 2b. In this scenario is an un-manned aerial vehicle (UAV) e.g. equipped with an imaging laser sensor system or a passive infrared imaging sensor. The image information from the UAV is transferred to a soldier using a portable transceiver capable of extracting the information from the retromodulating receiver on the UAV. If the laser in the transceiver can be intensity the modulated information can be transferred to another optical receiver using the soldier as a relay node. The retromodulating receiver is of particular interest in UAV applications due to the limited amount of available space, power requirements and weight. One critical parameter in the UAV scenario is the field of view of the retromodulating receiver.

Table 1 Example of military scenarios for retromodulating free-space optical communication.

Scenario	Data type[a]	Comments
Ground-to-ground	Sensor data, image information	Communication between vehicles, short distances, portable or mounted
Ground-to-air	Sensor data, IR-camera, high resolution, laser sensors for 3D imaging, TV-images	Retromodulating receiver on airborne platform
Air-to-ground	Ground sensor	Retromodulating receiver on ground,
Underwater	Sensor data	Short range communication, stationary or moving retromodulating receiver

a) Data rates of the order 10 Mbit/s or more are needed in future applications.

Another scenario is air-to-ground where the retromodulating receiver is located on the ground. The receiver could be mounted in a stationary location or on a moving platform, for example, a fighting vehicle. The airborne platform could be an UAV or a helicopter furnished with an interrogating laser transceiver with scanning and tracking capabilities. An optical beacon on the retromodulating receiver simplifies link establishment and

tracking performance. The tracking and scanning requirements depend on several parameters such as transmission time, retromodulator field of view, laser beam divergence, platform velocity and trajectory etc. The course tracking can be managed using a passive imaging sensor situated on the airborne platform. One interesting application in the air-to-ground scenario is communication from the airborne platform to a buoy situated on the water surface enabling communication to a submarine.

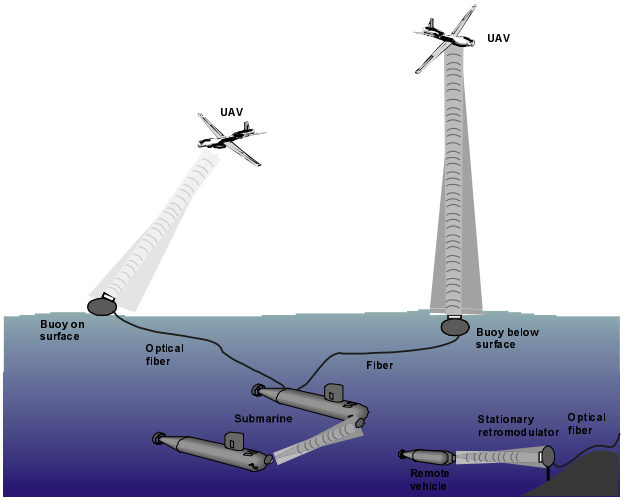

Figure 3. Example of underwater applications involving retroreflective free-space optical communication.

An important capability of a future submarine system is the ability to communicate rapidly utilising high data rates. The communication should be secure to prevent revealing of the position of the submarine. Un-manned underwater vehicles (UUV's) can be used for advanced surveillance and information from the UUV's sensors needs to be transferred to the submarine and to the control and command organisation. Free-space optical communication based on retromodulating techniques offer new possibilities to transfer information in submarine applications. Examples of scenarios involving a retromodulating receiver are depicted in figure 3. As discussed above one challenging application is to establish an air-to-surface communication link where the retromodulator is located on a buoy at the sea surface or slightly below the surface. In this application the retroreceiver probably needs to be stabilised on the buoy. For underwater applications is the range significantly reduced due to scattering and the applicable wavelength region is between 350 to 550 nm. The limited wavelength region puts constraints on the technology used for retromodulation. However, short distance links based on retromodulating principles provide simple communication without physical contact between platforms or a single platform and a stationary retromodulating receiver. Communication from vessels to submarines, to airborne platforms or between vessels can also be imagined.

Identification of individual soldiers and smaller platforms is an important task in future conflicts. The communication techniques described in this paragraph provide a simple method to transfer information after identification. A coded signal can be transmitted to open the retromodulating communication channel, subsequently, identification and information can be obtained simultaneously. Preferably, an electronic shutter is used to open the retromodulating receiver after the correct code have been identified by a laser warning device. In general, the retromodulator should be furnished with an electronic

(electro-optical) or mechanical shutter to prevent discovery. Depending on the military application and the tactical scenario different design aspects of a retromodulating communication system need be considered. Important issues are related to application wavelength, data transfer rates, field of view, data transfer times, pointing and tracking requirements. The complexity of the system is also linked to the application. For example, a hand-held portable system should be technical simple and have low weight and volume. On a larger platform, on the other hand, more complex solutions may be considered. The simplest type of system can be realised when a stationary or quasi-stationary platform is used for the retromodulating receiver.

3 LIQUID CRYSTAL SPATIAL LIGHT MODULATORS

Until now, dynamic multiphase-only modulation by means of liquid crystals has essentially been restricted to nematic devices, and such devices are commercially available. However, the requirement for higher speed (~10 kHz) has in later years directed the interest towards polar liquid crystals such as ferroelectric liquid crystals (FLC's). Commercial FLC spatial light modulator devices have been developed for binary phase modulation but the goal is, generally, to achieve analog phase-only modulation or at least four levels of phase. In this section FLC and antiferroelectric SLM's are discussed. Properties and applications of liquid crystal SLM's based on nematic materials have been discussed previously[7],[9].

For analog phase-only modulation, the most studied system comprises a half-wave plate, with an optic axis direction, electrically controllable in the plane of the LC cell, working with circularly polarised light. Electro-optic effects giving this geometry are for instance the electroclinic effect in the SmA* phase and the flexo-electrooptic effect in the cholesteric phase[7]. Moreover, the deformed helix effect in short-pitch SmC* materials, and the so-called V-shaped (analog) effect in surface-stabilised FLC materials, can with some approximation also be considered to give this electrooptic geometry, although the birefringence of the LC layer changes with the applied electric field. This effect gives a distortion of the circular polarisation depending on the wanted phase shift of each pixel of the SLM. However, the problems of LC alignment and the limited achievable deflections of the optic axis are still to be solved for this analog phase-only modulation.

One interesting approach is to work with four levels of phase by stacking two one-dimensional (1D) binary 256 FLC SLMs in series, i.e. mapping the first SLM giving 0° or 180° relative phase shift onto the second SLM giving 0° or 90° relative phase shift. In order to do this a special kind of high tilt FLC material, i.e. with a molecular tilt θ of approximately 45° have to be used.

3.1 Properties of high tilt materials

There exist few high tilt materials, i.e. with the tilt angle, $\theta > 42°$. The whole development of FLC materials has so far been directed towards materials with $\theta = 22.5°$ for FLC flat panels displays. The only commercially available material is Chisso-2005, with $\theta \sim 43^{o}$, which has been used for development of SLM's. The desired value would have been 45° but 43° gives essentially an equivalent performance.

3.1.1 Optical principle of high-tilt FLC SLM

The basic structure of a pixel-stripe of a prototype FLC SLM's is shown in figure 4[10]. The FLC material is arranged with the smectic layers perpendicular to the glass plates and the electric field is applied across the cell by means of applying voltages between the transparent electrodes (ITO) on the inner surfaces of the glass plates. The zero-field molecular organisation is controlled by certain polymer aligning layers on top of the ITO electrodes. On application of the electric field $\pm E$ the optic axis of the liquid crystal, defined by the average direction of the elongated molecules is switched between two positions, separated the angle 86° (~90°) degrees, in the plane of the cell. Linearly polarised light, polarised along one of those directions will experience a refractive index $n_{\perp}$ (perpendicular to the optic axis) for one polarity of the field and a refractive index $n_{//}$ (parallel to the optic axis) for the opposite polarity of the field. The relative phase shift that is achieved for light beams travelling through pixels subjected to different polarity of the field is $\delta = \frac{2\pi\Delta nd}{\lambda}$ where $\Delta n = n_{//} - n_{\perp}$ is the bi-refringence of the FLC material and d the thickness of the FLC cell. In order to get four levels of phase the first SLM corresponds to a half-wave plate and the second SLM to a quarter-wave plate[10].

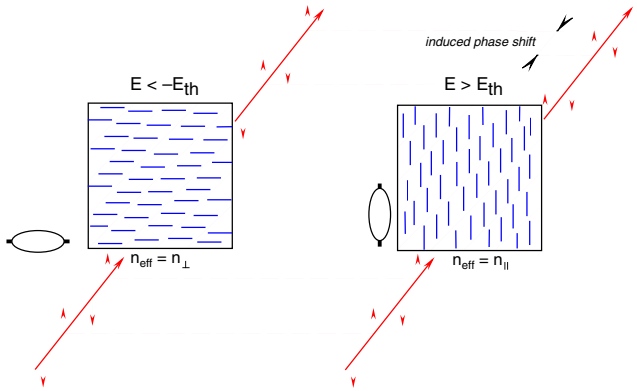

Figure 4. Basic structure of a SLM based on a high tilt angle FLC material.

3.2 Critical parameters

3.2.1 LC alignment

FLC materials are generally difficult to align in the desired 'bookshelf' structure inside the cell, i.e. with the smectic layers perpendicular to the substrate in a unique direction. In fact, the quality of alignment and the long term stability of the alignment under driving conditions is still the most severe and important problem to handle for any FLC device manufacturing. When using high tilt materials these problems are even more severe. Therefore, major efforts need to be directed to develop a new LC alignment scheme in order to accomplish a more homogeneous and more stable alignment of e.g. Chisso-2005. Initially, attention can be focused on new types of aligning layers and different combinations of rubbing directions and strenghts on the two substrates. It is well-known,

however, that unfortunately Chisso-2005 is extremely difficult to align in a homogeneous way over large areas and that the stability of the LC orientation is sensitive to asymmetric driving conditions[11].

3.2.2 Tuning of cell thickness

For good diffraction efficiency and complete extinction of the zero:th order extinction the thicknesses of the two SLM's needs to be tuned very precisely to constitute a half-wave and a quarter wave plate, respectively. In a non-industrial manufacturing process this is a serious problem and intrinsically a spread in thickness of the manufactured SLM's of the order of 0.1 to 0.2 microns can be anticipated. Accurate thickness can be accomplished using ”hard spacers”. If spherical plastic spacers are utilised a large amount of trial and error is required before the combinations of half-wave and quarter-wave plate SLM's which completely gives extinction of the zero:th order peak.

3.2.3 Mechanical stability

The system of two separate SLM's with pitch of 25 microns imaged onto each other is very sensitive to mechanical vibrations. A solution where the two SLM's are built on the same glass substrate could improve the mechanical stability. However, such a solution requires some adjustable mirror in the system and the exact adjustment of this mirror might be more severe than the adjustment of the second SLM with respect to the first. Furthermore, contact problems between the driving electronics and the SLM's via the so-called flex-prints have shown to deteriorate the performance of the SLM's.

3.2.4 User interface

The interface should be optimised with the emphasis to direct the steered laser beam to the retromodulator. The deflection angle should be adjustable using a feedback loop. This requires a capability to address all pixels individually. Additionally, DC compensation of the device must be sustained by utilising e.g., scrolling techniques.

3.3 Optimisation of performance

The following issues are most relevant for optimisation of the SLM performance:

- modification of the LC alignment layers in order to improve the diffraction efficiency, minimize losses and increase long term stability
- tuning of the SLM thicknesses for improved diffraction efficiency
- the beam steering SLM's should be adjusted to the operating wavelength used by the MQW modulators
- creating a user interface for directing the beam to hit the retroreflector.

3.4 Orthoconic antiferroelectric liquid crystal materials

New orthoconic antiferroelectric liquid crystal (AFLC) materials need to be studied and evaluated as materials for ternary (three-level) phase-only modulators. Ternary phase modulation decreases the theoretical diffraction efficiency compared to the quad phase (four levels) described above. However, as the three levels of phase is produced by only

one SLM in the orthoconic AFLC case, compared to two SLM's in the FLC case, an AFLC beam-steerer could be a competitive alternative. It has a number of attractive properties:

- only one single SLM is used – no imaging or vibration problems
- a passive matrix drive is generally possible, i.e. 2D SLM's could be constructed in the future (The Chisso-2005 material is monostable and requires direct drive or active drive.)
- reflective devices are possible, where the actual cell thickness is only one half of the effective thickness experienced by the light. This opens up for longer wavelengths, i.e. near infrared.

3.4.1 Orthoconic AFLC SLM for three level phase-only modulation

In AFLC's the molecules are arranged in layers similar to FLC's. Moreover, the molecules are tilted an angle θ with respect to the smectic layer normal and the tilt direction alternates (±θ) between adjacent layers. This structure is called anticlinic in contrast to the synclinic order characteristic for FLC. On applying an electric field perpendicular to the smectic layer normal of the AFLC material it can be switched into two synclinic ferroelectric states, where all molecules now tilt ±θ depending on the polarity of the applied field.The AFLC material can be arranged in bookshelf geometry, i.e. with the smectic layers perpendicular to the glass plates in a thin cell. The molecular tilt plane (in which the molecules tilt ±θ in adjacent layers) is parallel to the glass plates. In conventional AFLC materials, this presents a structure with an effective optic axis along the smectic layer normal, i.e. along the glass plates. On the application of an electric field between the glass plates the liquid crystal may be switched into its ferroelectric states, with the optic axis in the plane of the cell, tilted away from the smectic layer normal the angle ±θ, depending on the sign of the applied field.

Now consider an AFLC in which the molecular tilt angle is 45°. The optical properties of the bookshelf cell with the tilt-plane parallel to the substrates are now drastically changed. The zero-field state is uniaxial with the optic axis perpendicular to the tilt-plane and perpendicular to the glass plates. On the application of +E (-E), the liquid crystal is switched into its synclinic ferroelectric states, now having the optic axis +45° (-45°) from the smectic layer normal. Thus, *the effective optic axis can be switched between three orthogonal directions*, $E = 0$: optic axis perpendicular to the cell plane, $E > E_{th}$: optic axis in the plane of the cell, $E < -E_{th}$: optic axis in the plane of the cell, directed at right angle to the corresponding direction at $E > E_{th}$. Linearly polarised light, with its plane of polarisation at 45° with respect to the smectic layers, experience three different refractive indices depending on the value of the applied electric field (see figure 5). In conclusion a three-level phase-only modulator in one device has been accomplished[12],[13].

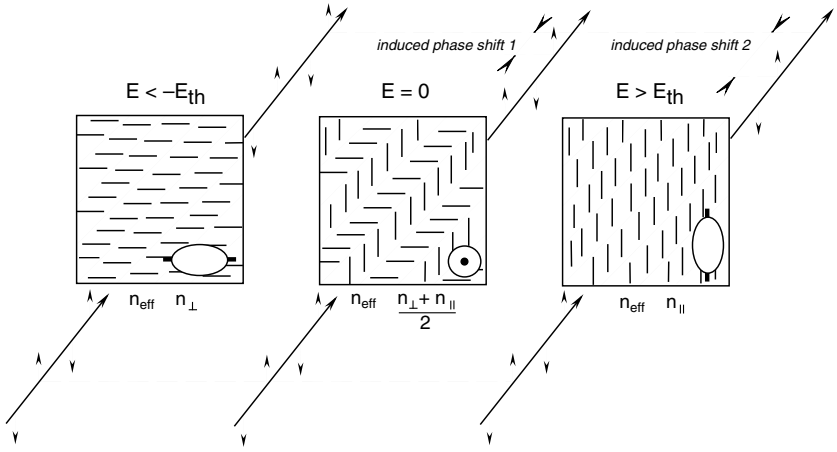

Figure 5. Optical properties of an AFLC in an applied electric field.

As AFLC materials are chiral they present a helical structure with a helix along the smectic layer normal direction in the bulk. In orthoconic devices this helical order must be suppressed which can be achieved in very thin cells, where the cell thickness is about the same or smaller than the intrinsic pitch of the helix. The first orthoconic materials had a very short pitch (~ 0.5 microns) and thus required submicron cell gaps to be helix free (surface-stabilised). However, in order to achieve a large enough phase shift in the three-level phase modulator a cell gap close of at least 2-3 microns for these materials is needed to achieve 0, 120 and 240° relative phase shift. In such thick cells the AFLC material is not surface-stabilised and the unique optical properties of the orthoconic AFLC materials are lost. Materials with larger pitch and/or larger birefringence are required in order to build a ternary phase modulator.

4 MULTIPLE QUANTUM WELL MODULATORS

4.1 Operating principles

4.1.1 Light modulation in semiconductor materials

Electro-absorption is a frequently used mechanism to modulate light that propagates in semiconductor materials. A simple picture is the following: photons whose energy is higher than the bandgap energy of a semiconductor material are absorbed, leading to the transition of an electron from the valence to the conduction band, while photons of lower energy simply propagates through the material (see figure 6). The principle of electro-absorption modulation is based on the decrease of the bandgap energy of a semiconductor due to the application of an electrical field. The electric field dependence of absorption at the band edge can be used to modulate the amplitude of light that propagates through the device. Applying an electrical field to a bulk semiconductor material can therefore turn it from transparent to opaque at a specific wavelength, thus achieving amplitude modulation of light, within 1 ns. However, the absorption spectra of semiconductor materials are actually not sharp edges, leading to poor modulation performance in terms of contrast ratios.

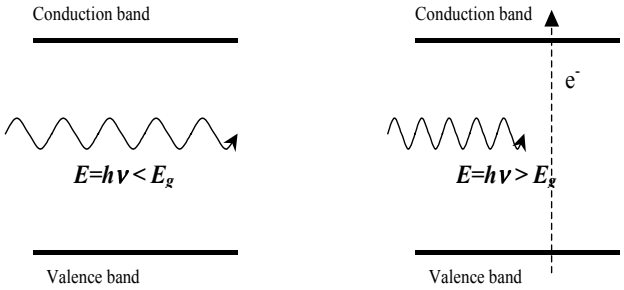

Figure 6. Light-matter interactions in semiconductor materials. Transmission (left) and absorption (right).

4.1.2 Electro-absorption in quantum wells

Electro-absorption can be made more efficient if quantum well structures are considered. A multiple quantum well structure is a stack of very thin layers of a narrow bandgap semiconductor material, also called wells, sandwiched between layers of a larger bandgap semiconductor material, the barriers. A schematic illustration of a multiple quantum well structure is provided in figure 7.

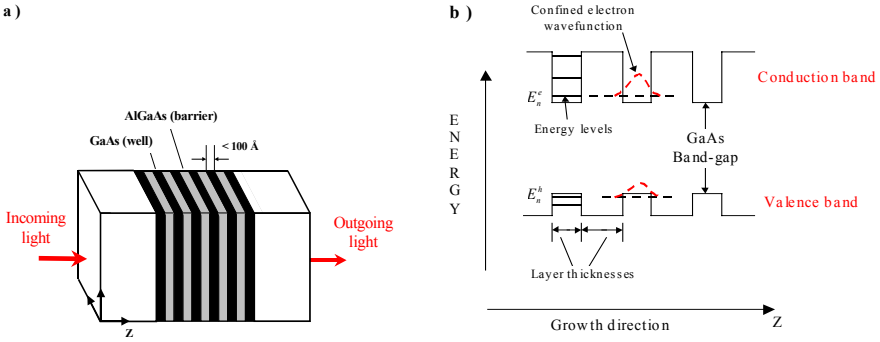

Figure 7. Schematic representation (a) and band diagram (b)of a multiple quantum well structure

In a quantum-well structure, the electron and hole motion normal to the quantum well layers are confined in space by the discontinuity in the structure and show one-dimensional behaviour whereas parallel to the layers the carriers can move with two-dimensional freedom. This reduced dimensionality, compared to bulk semiconductors, induces drastic changes in the electrical and optical properties of the semiconductor materials, which forms these quantum-well structures.

4.1.3 Excitons

In particular, while bulk semiconductors show a rather smooth energy dependence on absorption, the absorption spectrum of a GaAs/AlGaAs quantum-well structure seen in figure 8 shows features of step-like absorption edges and room temperature exciton resonances.

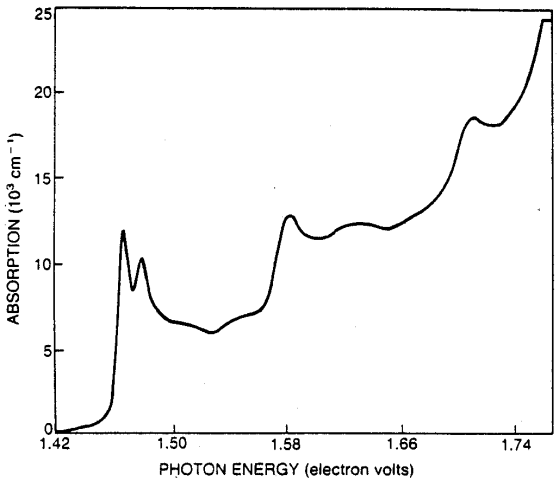

Figure 8. Absorption spectrum of a GaAs/AlGaAs quantum-well structure. The steps in the spectrum are a result of transitions between sub-bands. The peaks before the edge of the steps are due to excitons[14].

The step-like absorption edges are a result of the quantisation of the electron and hole motion perpendicular to the layers, which give rise to discrete energy subbands at energies E_n, n=1,2,3 (see figure 7 b). This quantisation changes the optical interband absorption to a series of steps. The interband absorption creates free electrons and holes. The absorption strength (corresponding to the height of the steps in figure 8) is proportional to the overlap integral (squared) for each hole and electron wavefunction of interest. The interested reader may found further description over absorption in quantum well semiconductors in refs.[15],[16].

The strong absorption peaks seen at the edges of the steps just below the interband absorption (i.e. close to bandgap energy) are due to electron and hole interaction. When a semiconductor absorbs a photon, an electron is raised to the conducting band leaving a hole left in the valence band. The opposite charges of the electron and hole give rise to Coulomb attraction between them. This results in a bound state of the electron and hole analogue to the hydrogen atom, where the electron and hole orbit round about one another. This bound state referred to as an exciton, lowers the threshold energy needed to cause absorption. The electron-hole interaction produces a set of discrete and very strong absorption lines just below the interband absorption steps. Due to the confinement in the quantum wells, the electron and hole are forced to orbit closer to each other, increasing the binding energy of the exciton by a factor of two to three. This added stability makes the exciton resonance observable at room temperature. In bulk semiconductor materials, the exciton peak is usually well resolved only at very low temperatures (18K in bulk GaAs), since they are easily broken apart by thermal phonons. Also, while in bulk GaAs only one exciton resonance can be distinguished, the reduced symmetry of quantum well structures separates the degeneracy, producing two valence bands and hence two excitons (heavy- and light-hole excitons). The electron-to-heavy-hole exciton is of larger interest for the use in intensity modulators, since it occurs at lower energies and shows much stronger absorption than the electron-to-light-hole exciton.

4.1.4 Quantum-confined Stark effect

Owing to the quantum confinement and the presence of excitonic effects, the electro-absorption effect in quantum wells is much stronger and manifests itself as a rapid variation of absorption spectra of quantum well structures when a field is applied transversally to the wells.

When an electric field is applied perpendicular to the quantum well layers, an effect specific to quantum wells occurs. The electric field pulls the electron and hole in opposite directions, but, as opposed to bulk mechanisms, the electron and hole are constrained to stay, within the well, close enough to remain bound. The lifetime of the exciton is determined from the probability that the electron tunnels out of the well each time it hits the barrier wall. This drastically increases the lifetime of the exciton and hence makes the exciton resonance peak clearly visible at room temperatures and at much higher fields than the classical ionisation field in bulk semiconductors. However, the pulling apart of the exciton wave function, which does occur, results in an increased exciton radius and therefore reduced Coulomb interaction which leads to a lowering of the resonance energy and reduced absorption due to the decrease in the overlap of the particles wave function. It is possible to apply fields that are two orders of magnitude larger than the classical ionisation field, inducing a shifts of the absorption peak toward longer wavelengths many times the binding energy, and still observe exciton resonance. This phenomenon has been termed the quantum-confined Stark effect (QCSE) and is the dominant electro-absorption mechanism below the interband absorption in quantum well structures[17].

QCSE enables an abrupt, highly absorbing edge to be shifted into a spectral region where the sample is normally transparent. The interband transition is also altered by the electric field. The conduction and valence bands are “tilted” and the electron and hole quantum well wave functions are pulled to opposite sides of the well by the field (see figure 9). The electron and hole wave functions are no longer orthogonal and hence many previously forbidden transitions now become allowed. This results in a lowering of the threshold absorption energy, which cause a shift of the absorption edge to lower photon energies. The overlap (integral) of the carrier wave-functions is also reduced, decreasing the absorption strength, and hence lower the height of the absorption steps.

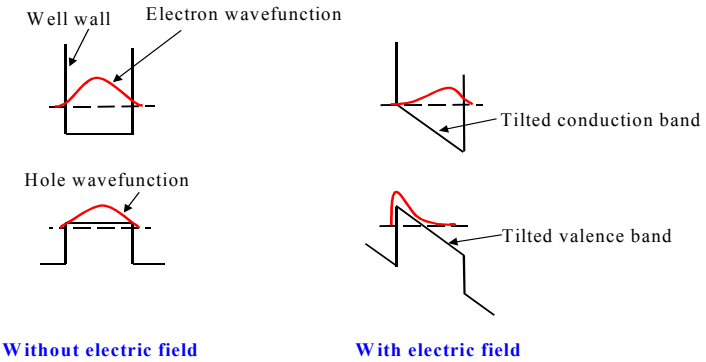

Figure 9. Electron and hole energy levels and wavefunctions in a quantum well with (right) and without (left) an electric field applied perpendicular to the QW layers. The field pulls the electron and hole in opposite direction, but the quantum well walls (barriers) holds the particles (excitons) in a bound state.

The main features of the QCSE, as illustrated on figure 9, are therefore:

- the shift of the absorption edge towards lower photon energies (longer wavelength) with applied electrical fields
- the fact that the exciton absorption peaks remain resolved for a considerably large shift and in room temperature.

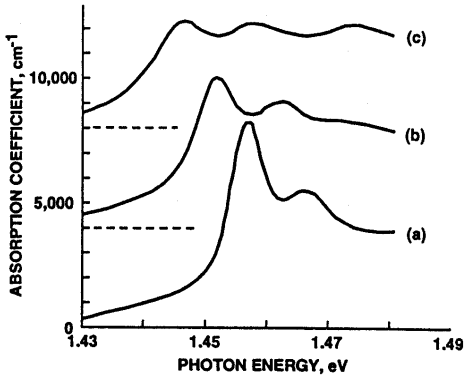

Figure 10. Quantum confined Stark effect in GaAs/AlGaAs MQW structure with various applied electric fields perpendicular to the quantum well layers: (a)1.4×10^4 V/cm, (b) 4.7×10^4 V/cm and (c)7.3×10^4 V/cm. The spectra are shifted vertically for clarity.[14]

Waveguide electro-absorption modulators are nowadays often used in optical communication systems to transmit information. Transversal modulators benefit from the large change in absorption of light propagating perpendicularly to the surface of the structure and can be fabricated in two-dimensional arrays and their large apertures are well-suited to free-space architectures[18].

4.1.5 Electrorefraction

In addition to absorption changes in quantum wells, an accompanying phase change of the propagating light occurs. This phase change is a result from refractive index changes in the quantum well material that are coupled to the absorption change as described by the Kramers-Kronig relation. The relation can be written as

$$\Delta n(\lambda, V) = \frac{1}{2\pi} P \int_{o}^{x} \frac{\Delta\alpha(\chi, V)}{\left[1 - \left(\frac{\chi}{\lambda}\right)^2\right]} d\chi \qquad (1)$$

where P is the Cauchy principal value of the integral and V the applied voltage[19]. Consequently, the QCSE can be used to modulate both the amplitude and phase of light.

4.1.6 Theoretical models

An example of simulated electro-absorption in quantum wells is shown in figure 11a. A clear and well-defined absorption peak, due to the presence of exciton states in quantum wells, can be seen at room temperature without any applied field. When an electrical field is applied transversally to the wells, the excitonic absorption peak is shifted to longer

wavelengths. Since the confined electron and hole related to the exciton move in opposite sides of the well, the excitonic peak decreases in intensity. The peak remains resolved and significant broadening only occurs at high electrical fields. Changes in refractive index of an AlGaAs/GaAs multiple quantum well structure for various fields is shown in figure 11b.

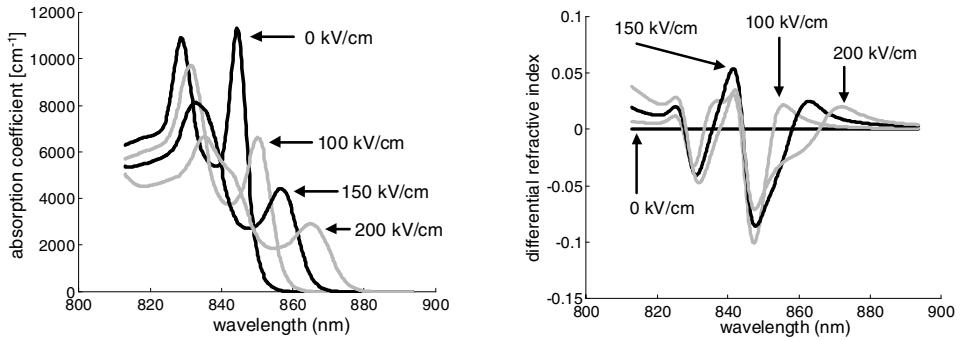

(a) (b)

Figure 11. (a) Simulated absorption coefficient and (b) differential refractive index of an AlGaAs/GaAs Multiple Quantum Well structure.

4.1.7 Modulator design

The structures are modelled in one dimension only (the depth), which means that no lateral effect (pixellation, for example) is taken into account. Although it could be modelled, phase behaviour is not looked at either. The main idea, which the modulator structure design is based on, is the constructive/destructive interference phenomena occuring in a Fabry-Perot cavity, resulting in a highly non-linear behaviour of the reflectance/transmittance of the cavity with regards to such quantities as wavelength, cavity length or cavity absorption. We use quantum wells inside the cavity to modulate the absorption by a change in electric field. The structure as seen from an optical standpoint is shown in figure 12.

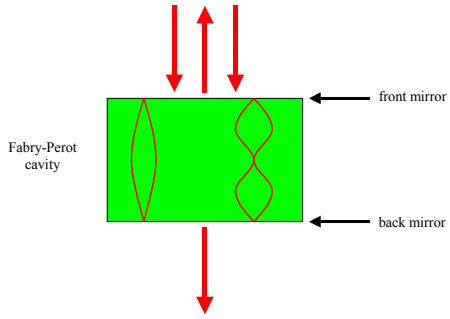

Figure 12. Sketch of a Fabry-Perot cavity, as used for the optical modulators.

From an electrical point of view, the semi-conductor structure is a reverse-biased p-i-n diode. The front- and back-mirror are located in the n- and p-doped regions respectively, while the intrinsic region and possibly the inner part of the doped regions constitute the optical cavity. The quantum wells are located in the intrinsic region. This configuration allows us to change the electric field seen by the quantum wells (by changing the bias of

the diode) and thus to vary the absorption inside the cavity. Because the diode is reverse-biased, the current and therefore the total electrical power is kept low. The layout of TS2, one of the structures we have grown, is shown in figure 13 as an illustration.

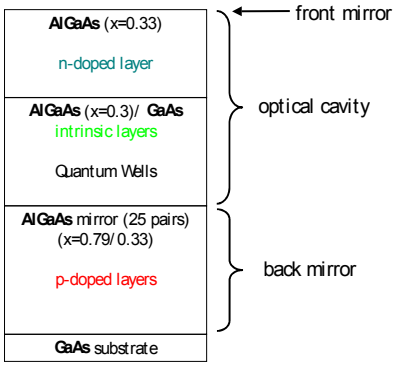

Figure 13. Layout of the "TS2" structure.

The principle of the modulator is based on the possibility to change the absorption inside the cavity. A simulation tool, IGAP, which computes optical properties (absorption and change in optical index as a function of the wavelength and the external electric field, see figure 11) of any III-V-based quantum well superlattice is used. We choose the superlattice based on, amongst other things, the wavelength region we want to use.

A simulation of the passive behaviour of the optical cavity is done using a set of Matlab routines. These routines use optical impedance transfer matrices to compute the reflectance of the structure and allow to adjust the thickness of most layers in a minimum time. The optical indices are wavelength-dependent and interpolate between published values. Absorption from the quantum wells is, however, not taken into account at this stage. These routines are a very flexible tool to evaluate different layouts in a very short time.

Once satisfied properties of a given passive cavity are obtained, a more accurate simulation model to look at the active behaviour of the structure is used. This simulation tool is known as *newspc*. It is based on a model solving the Maxwell equations inside the structure. It computes the reflectance of the structure as a function of the applied electric field for a range of wavelengths. Other optical properties, such as the phase shift, can also be computed. This is usually the last step in the optical design itself. The design steps are shown in figure 14.

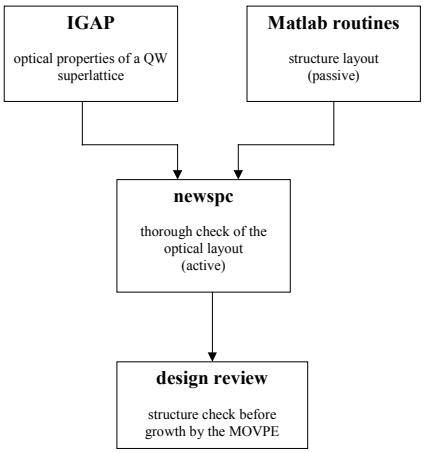

Figure 14. Scheme of the design steps of a MQW modulator.

4.2 Fabrication process

4.2.1 Fabrication of amplitude modulators

Many demonstrations of MQW modulators are using GaAs and AlGaAs for the wells and the barriers, respectively. This material system is now mature and is a viable technology for production of high-quality components. Due to the resonance nature of the quantum confined Stark effect, only a narrow part of the spectrum is significantly modulated, as shown in figure 11. Quantum well devices have therefore a narrow spectral bandwidth, which can be however tuned by varying the thickness of the wells. For GaAs/AlGaAs devices, operating wavelengths can be chosen between approximately 800 and 870 nm, which is compatible with coherent optical processing applications. Other material systems can be used to reach other wavelength ranges of interest, such as InGaAs/GaAs between 950 and 1060 nm and InGaAs/InP for telecommunication wavelengths.

Based on the design discussed above for amplitude modulation, a first epitaxial structure was grown. The 4'' GaAs wafer with SLM structures grown by MOVPE has been cleaved into several 16 x 20 mm^2 chips. In order to define mesa, p and n contacts, three masks (shown in figure 15) were designed and fabricated.

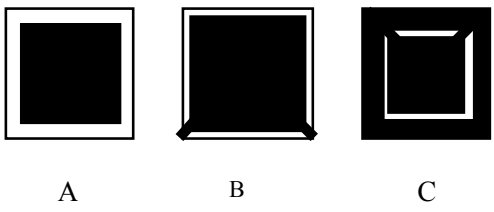

Figure 15. Mask set for the fabrication of the amplitude modulator chips

The first mask (A)was used to define the "mesa": the outer frame was etched to reach the p-doped layer, which is needed to process contacts on the p side. The inner square became a mesa, that is to say a plateau, the top of which is made of n-doped material. Metallic

contacts are processed on the p-type area using mask (B) and on the n-type area using mask (C). After processing, each chip was mounted to a chip carrier and wire bounded to the carrier pads. A completed modulator and its cross-section are shown in figure 16.

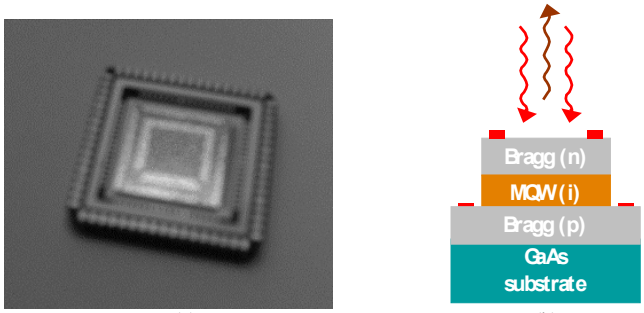

Figure 16. Amplitude modulator chip(a): Photo of an experimental chip and (b): Schematic side-view representation

The whole processed area is a 13.5 x 13.5 mm^2 square and the mesa is 10.5 x 10.5 mm^2. The p-contact frame is separated into a U-shape part and another part, which makes it possible to check the quality of the contact by measuring the I-V characteristic of the p-p contacts. For the same reason, the metallisation on the n-doped area is separated into a U-shape and a bar.

The fabrication process is summarised below:

1. Lithography to define the mesa
2. Wet etching H_3PO_4:H_2O_2:H_2O
3. Lithography to define the p-contacts
4. Evaporation of Au/Zn/Au and lift-off
5. Lithography to define the n-contacts
6. Evaporation of AuGe/Ni/Au and lift-off
7. Annealing
8. Wire bonding

4.3 Drive electronics

4.3.1 Electrical properties

MQW modulators are most commonly fabricated as p-i-n diodes to allow external control of the applied electrical field. Absorption in MQW modulators relies on carrier transitions from the valence to the conduction band in direct semiconductors. It is a very fast effect, the speed of which is practically limited by the RC constant of the device. Its response time is in the sub-nanosecond range.

With the current device design, the capacity is

$$C = \frac{\varepsilon_o \varepsilon_r S}{d} \approx 10 - 20nF \qquad (2)$$

where ε_0 is the permittivity of air ($\approx 8.85 \times 10^{-12}$ F/m), ε_r is the relative permittivity of AlGaAs (≈ 13), S is the mesa area (10^{-4} m^2) and d is the depletion length (10^{-6} m)

The device resistance highly depends on the quality of the ohmic contacts, which in turn depend on the doping concentration in the n- and p-doped regions. The contact resistance, ranged from good ohmic contacts ($\approx 50\ \Omega$) to Shottky contacts exhibiting a much higher resistance. However, there is no fundamental limit @50Ω and the contact resistance should decrease when the doping level is further improved. A device resistance of 50 Ω sounds a reasonable expectation. To improve the response speed of the device (if necessary), it is possible to pixellate the modulator, making a matrix of modulators which decreases the total capacitance.

4.3.2 The driver

Standard drivers have an internal output of 50 Ω. Since this resistance will be in series with the resistance of the modulator and both are of the same order of magnitude, the driver will increase the RC constant of the whole circuit and slow down the modulator. To avoid this slow-down, a low-impedance amplifier must be used between the modulator and the driver, as shown in figure 17. The amplifier shall have an internal resistance of 1 to 2 Ω.

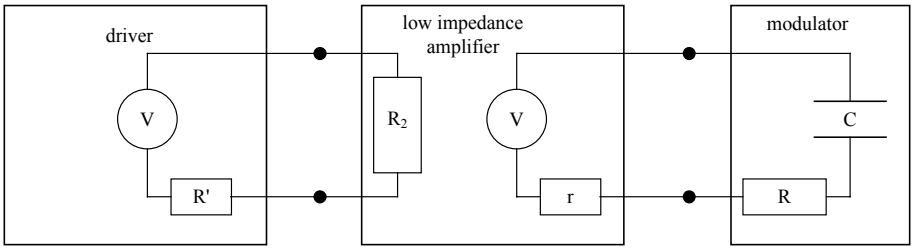

Figure 17. Electrical setup to drive the modulator. A low-impedance amplifier is used to avoid adding a high resistance in series to the modulator.

5 TECHNIQUES FOR LINK ESTABLISHMENT AND TRACKING

In the retro-communication system a laser beam is to be directed towards a retro-reflecting target, where a message is imposed on the retro-reflected beam by a fast modulator as described above. The laser transmitter should preferably be able to address several targets and the targets should furthermore be allowed to change their positions. Consequently, the laser transmitter unit (transceiver) should be capable of directing the laser beam in arbitrary directions within its operating angular span and also to dynamically change the beam directions when the targets move, i.e. to track the targets.

What does it take to deflect the laser beam a certain angle φ? The answer is simple: Provided that there is no focusing connected with the deflection it simply takes an imposed linear phase shift across the beam at the (spatial) rate $2\pi/a = 2\pi\sin\varphi/\lambda$, where λ is the laser wavelength. The traditional way of imposing a linear transverse phase shift to achieve beam deflection is by means of a planar mirror or a prism. Acousto-optic

deflectors and micro-lens arrays, moved by piezo transducers, are more recent (and complicated) devices for the purpose. An overview of current and anticipated future beam deflection devices can be found in a previous study[7].

For several reasons, in this project we decided to employ electrically controlled, pixelated spatial light modulators based on liquid crystal material, operated in phase modulating mode, for beam deflection. These SLM's have the desirable features of low power consumption and random deflection capability. Also they are reasonably small and low weight. Their speed is only moderate, though, LC SLM's of ferro-electric type with switching times in the microsecond range and those of nematic type in the millisecond range. Whereas FLC SLM's are binary phase valued, often with a phase modulation step of π radians, nematic SLM's are continuously variable and may take on any phase-shifting value between zero and 2π radians. However, in practise the driving electronics of nematic SLM's only provides a limited number of phase levels, e.g. 64.

The fact that the LC SLM's are pixelated means that the phase structures they can synthesize are stair-like instead of linearly sloping, as they ideally should be. The phase quantization of practical LC SLM's mentioned further restricts the accuracy of the stair-like approximations to the intended linear phase shifts. Some properties of stair-like phase structures are discussed below. Apart from steering light in the intended direction these phase structures diffract light in other directions. For instance, a binary phase grating structure steers a maximum of 40.5% in the intended (first diffraction) order. The same amount of light power also gets diffracted in the other first order. In figure 18 power fractions diffracted in different orders for a few diffracting phase stair gratings are shown.

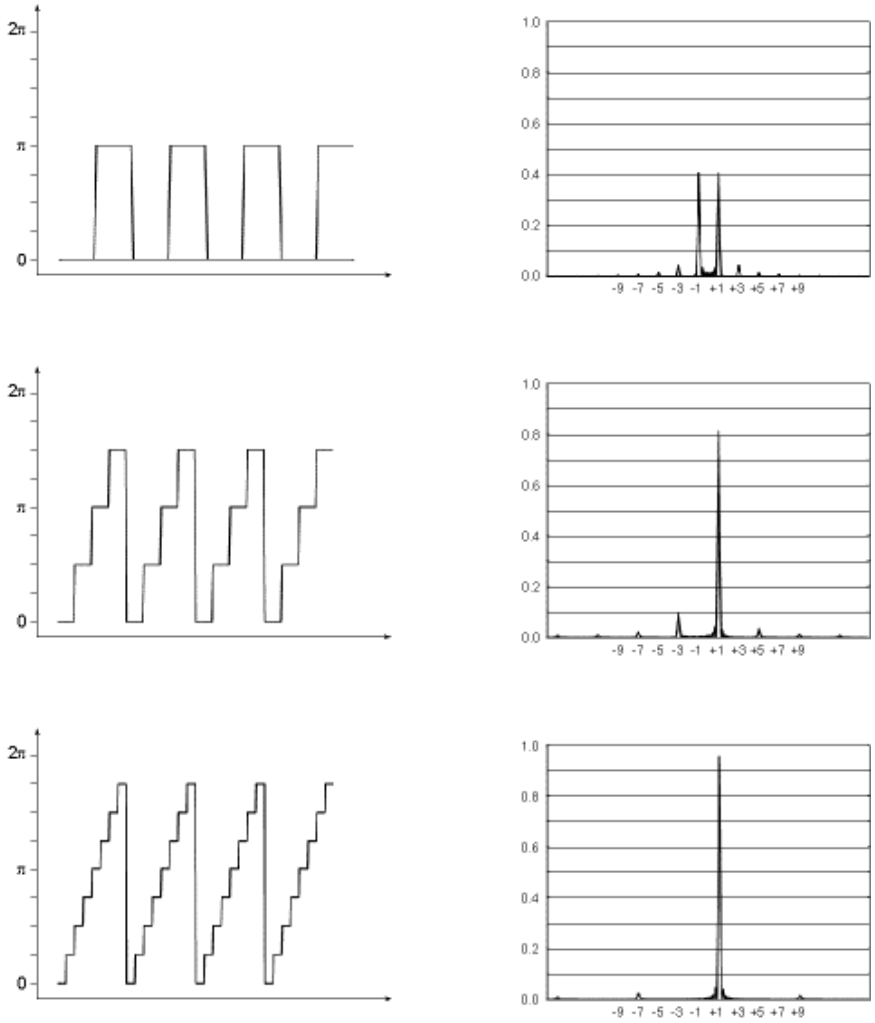

Figure 18. Three examples of stair phase approximations to a blazed grating with (top) two, (middle) four and (bottom) eight phase quantization levels.

Besides a reduced power in the intended direction, i.e. limited diffraction efficiency, the fact that power gets steered in unwanted directions also represents a directivity ambiguity of the beam steerer. A practical, yet relatively accurate estimate of the power fraction diffracted in the first order, η, is given by the following expression:

$$\eta = e^{-\sigma^2} \tag{3}$$

where σ is the rms-phase deviation between the actual and the intended (in our case linear) phase profile.

It is further to be noted that the phase quantization puts a limit to the angular accuracy of the steered light. Provided that the number of pixels in the SLM is several hundred, which it typically is, the angular inaccuracy due to the phase quantization is minor, however, but in micro-scanning mode, when the scanning step is just a fraction of the diffraction beam, the effect is significant. Below we report on some initial experiments on micro scanning performed with a binary FLC SLM. A common effort is try to exploit the speed of FLC while avoiding the limitations set by its binary nature. By cascading two binary FLC SLM´s so that the first SLM is coherently imaged onto the second with perfect scaling and

matching, pixel by pixel the number of phase steps are increased. The first SLM has a phase modulation step of π, the second a step of π/2. That way "synthetic" four level phase structures can be realised. A schematic of the optical set-up is shown in figure 19.

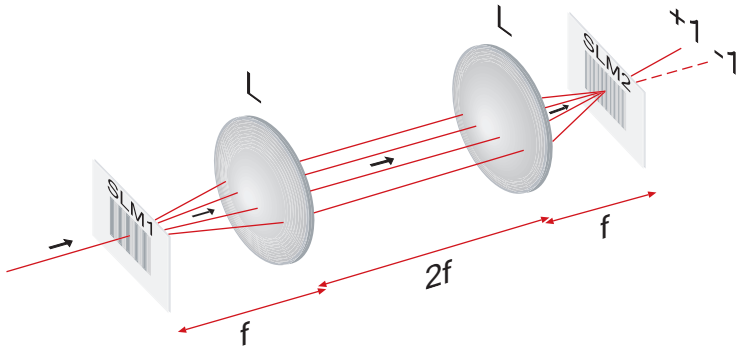

Figure 19. Coherent imaging geometry of a four-phase level beam steerer. The modulation steps of SLM1 and SLM2 are π and π/2, respectively.

Using two FLC SLM's the scheme shown in figure 19 was evaluated in a first set of experiments. Using simplified, but inflexible driving electronics reasonably good beam steering was demontrsated, in a way which clearly displayed the characteristics of synthetic four phase level diffraction, c.f. figure 20. By comparison with figure 18, note that the measured power fraction in the second most powerful order (the 3rd order on the "other side" of the zero order) is about three times that of an ideal four-phase level grating. Simulations show that this caused by the dead space between pixels and that a reduction of the dead space from its present value of 5 µm to 2,5 µm would reduce the unwanted power in the third order by about 40%. The power appearing in the even orders (c.f. figure 20), but which is absent for an ideal four-level phase grating (c.f. figure 18), should be due to the periodic amplitude modulation that the ITO-electrodes of the pixels of the SLM's gives rise to.

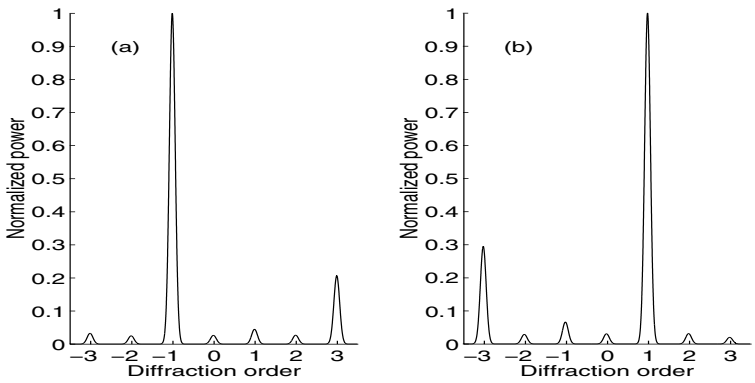

Figure 20. Measured optical power in central diffraction orders by the two-SLM scheme, the SLM´s set to generate a (left) left- and (right) right-handed four phase approximation of a blazed grating. Optical wavelength: 543 nm.

In a separate experiment the phase modulation depth as a function of wavelength was measured for both SLM´s, one at a time. The measurements showed that the intended phase modulation depths of π and $\pi/2$, which were to be reached at the wavelength 633 nm, in fact occurred at the wavelengths 570 nm and 475 nm, respectively. Simulations indicate that the measured wavelength mismatch has significant but no dramatic influence on the performance of the four phase level beam steerer: The diffraction efficiency drops from a maximum of 81% (c.f. figure 18) to 73% and 70% for the operating wavelengths 543 nm and 633 nm, respectively.

New flexible driving electronics for the FLC SLM's, so that arbitrary four-level phase structures can be generated with the SLM's are under development. This ability is of course necessary for link establishment and for subsequent tracking. Using the upgraded electronics tracking experiments with feed-back signals from a position sensitive detector that measures the location of the steered beam will be carried out.

Recently initial experience on link establishment and tracking was gained using an existing re-configurable 1 x 8 optical switch, which has a reflective FLC-on-silicon-SLM at its center, and was made adaptive by introducing feed-beck. In the switch, schematically shown in figure 21, the signals are carried on single-mode fibers, the switch able to couple the input signal into any of the eight output fibers. Feed-back is obtained by tapping part of the power from the output fibers, a computer using the out-coupled power to dynamically calculate and display holograms on the SLM.

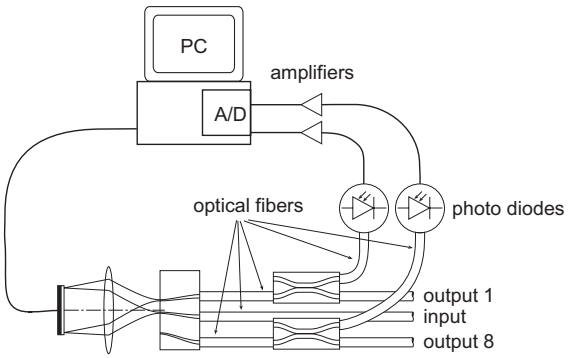

Figure 21. Schematic of the studied adaptive free-space optical switch.

To have reasonably long lifetime FLC SLM's need to be "DC-balanced", which means that over a time-span of about 10 ms the average voltage over any pixel should be zero. In the experiment we ensured DC-balancing by periodically interchanging a hologram for its inverse. The method is simple but has the disadvantage that during the switching the hologram is "blanked" for a short while so that the connection the beam constitutes temporarily gets broken. To maintain connection DC-balancing can alternatively be ensured through hologram scrolling, which requires considerably higher up-dating frequency, though.

The ability of the system to perform micro-scanning, i.e. to direct the beam in angular steps much smaller than the diffraction limited beam, was tested by calculating and displaying a sequence of holograms that steered the beam toward the end of a receiving

fiber (wave-guide in actuality) and to measure the in-coupled power. The result, presented in figure 23, indicates successful microscanning. The estimated beam steering uncertainty in the experiment is only about 6 µrad.

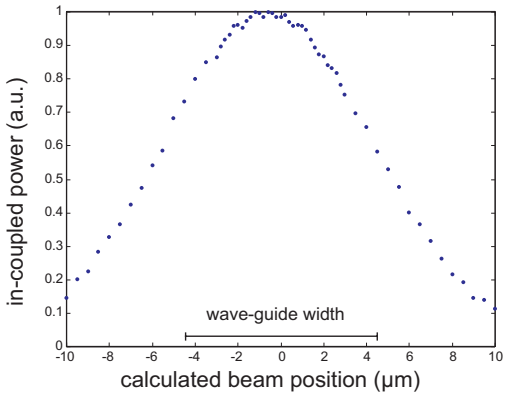

Figure 22. Result from micro-scanning a focused beam across a receiving wave-guide

What algorithm should be chosen to calculate holograms is not obvious. However, the holograms it calculates should steer the beam in the intended directions with high accuracy and it should further be fast enough to allow calculation "on the fly", which means it must be simple. The method we used in the experiment is indeed quite simple: Starting with a known, target deflection angle, which defines the constant phase rate across the beam, the pixels are sequentially given individual phase values out of those available (two in this experiment) so that the phase deviation from the ideal linearly varying phase is minimum for each pixel. The procedure minimizes the rms phase deviation between the synthesized hologram and the ideal linear phase profile, and hence maximizes the diffraction efficiency. Alternative approaches can be considered and will be studied further within the project.

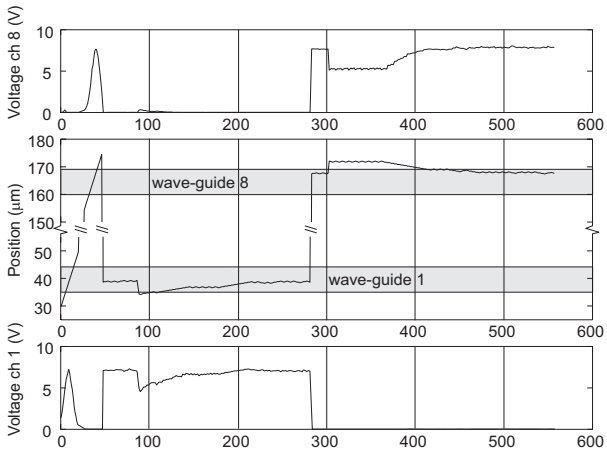

Figure 23. A sequence of data sampled when running the active alignment system.

Using our simple algorithm with the system shown in figure 21 we carried out a first adaptive beam steering experiment in which a controlling computer first localized the positions of two receiving fiber ends, then locked to them by slightly varying the deflection angle, using the measured in-coupled power for feed-back signal. The

experiment, during which we made two deliberate misalignments, one at time 90 s, another at time 300 s, is graphically shown in figure 23. Active locking to a fiber is shown in figure 24.

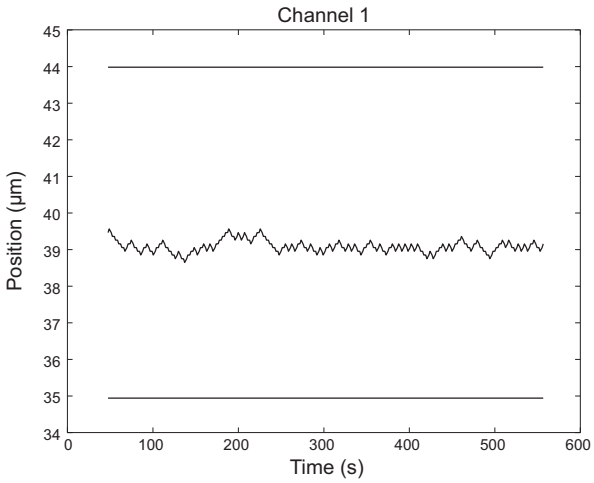

Figure 24. Active locking to a fiber end.

6 SYSTEM ARCHITECTURES

Several system architectures need to be considered in designing a retroreflective free-space optical communication link. Basically the link can be divided into two major parts; the transceiver containing the laser source and an optical receiver and the retromodulator. An additional optical receiver can be implemented together with the retromodulator to provide an identification channel which starts the transmission via the retromodulator. The purpose of this paragraph is to discuss different architectures and parameters which affect the performance. The operating principles for the different sub-components are also examined and reviewed. Advantages and disadvantages of different system configurations are discussed.

6.1 Transceiver

The transceiver in a retroreflective optical communication system can be divided into different parts as mentioned above. The transceiver assembly consists of the interrogating continuous wave (cw) laser, the optical receiver and the beam steering unit. Two different configurations of the transceiver design can be imagined. In a mono-static configuration the optical axis of the laser source and the optical receiver is bore-sighted. The major advantage with a mono-static system is that alignment errors are reduced and tracking- and search principles are simplified. In a bi-static configuration, on the other hand, the optical receiver and the laser have separated optical axis. From a technical point of view is the bi-static optical configuration simpler in comparison to the mono-static. In the mono-static transceiver a central part of the optical receiver will be blocked if a Cassegrain telescope design is used.

The optical receiver should be isolated optically from the laser source in order to reduce the stray-light and lower the optical noise. A tracking and acquisition sub-system is also necessary in order to provide feedback information to the beam steering device. Coarse

beam steering is probably performed by using ordinary mirrors since the maximum deflection angle of the fine beam steering device is limited (order of degrees). An example showing hypothetical transceiver arrangements is depicted in figure 25. It should be noted that no tracking and acquisition sub-system is implemeted in this example.

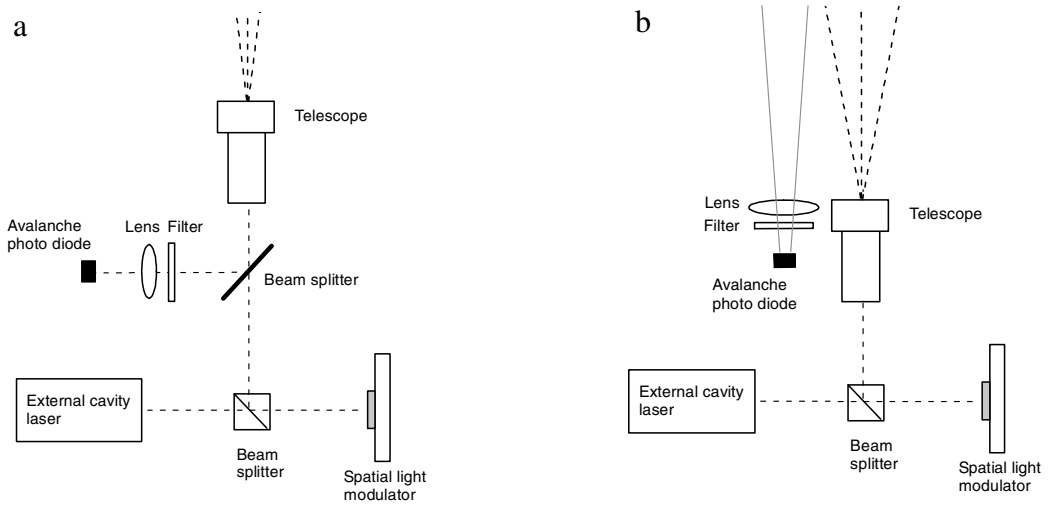

Figure 25. a) Schematical layout of a transceiver (mono-static system) in a retroreflective free-space optical communication system. b) Same as a) but in a bi-static arrangement.

6.1.1 Laser source

Optical modulators based on the principle of electro-absorption (or the quantum confined Stark effect) exhibit a narrow optical bandwidth, usually of the order of 1 nm. The linewidth of the interrogating laser and the uncertainty in central laser wavelength should consequently be less than the optical bandwidth of the MQW modulator.

A cw laser is utilised to extract the information from the retromodulating receiver. Several candidates exist depending on the operating wavelength of the modulator. MQW modulators based on the material combination AlGaAs/GaAs have an operating wavelength about $\lambda = 850$ nm. However, the wavelength may slightly be shifted to higher or lower values depending on the design parameters of the modulator. The most suitable candidates for laser sources operating about 850 nm are AlGaAs/GaAs laser diodes. They have high output power and commercial devices with output power up to 200 mW are available. These diodes are constructed using a Fabry-Pérot cavity with a cavity length of approximately 100 µm. The spectral bandwidth of this type of laser diodes is usually of the order of $\pm$ 3–5 nm. Since the operating center wavelength may vary as much as 10 nm between individual diodes a selection procedure is required. Vertical cavity surface emitting lasers (VCSEL) can also be constructed to operate in a narrow band at the desired center wavelength. They suffer from limited output power (~ 1-5 mW) and is not suitable for an application such as a retroreflective free-space optical communication link.

After selection of an appropriate laser diode a technique to filter out or tune the laser to the specified center wavelength is needed. A narrow-band Bragg filter may be used to select the correct center wavelength. However, using an external cavity laser the wavelength can be tuneable over a wider wavelength region (~ 10 nm) with a small line

width (5-25 MHz). Two common different designs of external cavity lasers are shown in figure 26. In the Littrow design is the feedback to the Fabry-Pérot cavity in the laser diode accomplished by the first order diffraction peak from the grating. The cavity length is increased and single-mode operation can be obtained. The tuning mirror can be neglected with the disadvantage that beam wander occurs during wavelength tuning. The rear side of the laser diode is coated with a high reflectivity mirror forming the end mirror of the cavity. The Littman design (figure 26b) has a smaller line width in comparison to Littrow. An additional etalong is introduced to improve the line width but makes the design more complex. In the case of retroreflective optical communication an external cavity laser using the Littrow cavity concept is adequate. The extra tuning mirror can also be neglected if smaller beam displacement can be accepted.

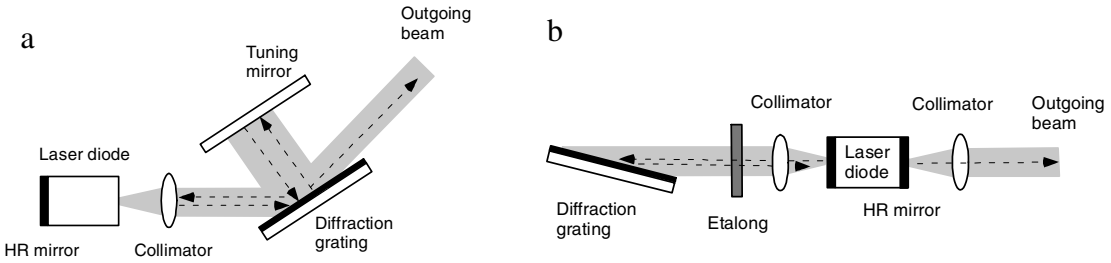

Figure 26. a) Littrow and b) Littman cavity designs.

One delicate problem to consider using semiconductor laser diodes is mode hopping. Mode hopping causes temporal fluctuations of the output power and spatial alterations in the beam profile. Mode hopping effects can be suppressed by carefully adjusting the injection current to the laser diode and stabilising the ambient temperature. Further improvement can be achieved with a regulator circuit and a piezoelectric scan control. Mode hopping is of importance in communication applications since alterations of the modes cause power fluctuations, which may introduce bit errors in the transmitted signal.

A diffraction limited laser beam is desirable in free-space propagation applications. The lowest Gaussian mode, TEM_{oo}, is usually assumed to be valid for model calculations. Laser diodes suffer from degraded spatial beam profiles and astigmatism making the beam profile elliptical in shape. The elliptical beam profile can be corrected by an anamorphic prism pair. An improved beam profile is obtained by coupling the light from the laser diode into an optical fibre which carefully filter out unwanted high-order spatial modes.

6.1.2 Optical receiver

The optical receiver consists of the reciver optics, i.e. optimised to collect the irradiation reflected from the retromodulator, and the detector with corresponding amplifier. One important design parameter for the receiver is the field of view (FOV). The field of view is given by the detector area and the effective focal length of the optical receiver. Different designs of the optical receiver need to be considered studying free-space optical communication. One critical issue is to optically isolate the laser source from the receiver optics to reduce effects of stray-light.

6.1.2.1 Optical design

Several optical configurations of the receiver optics can be imagined. The most simple configuration is to use a bi-static system as outlined in figure 25b. In this case a large aperture lens is used to collect the modulated light reflected from the retromodulator. The overlap between the optical receiver field of view (Ω_r) and the laser beam divergence (θ_l) affects the required accuracy for the tracking process. One disadvantage of the bi-static configuration is the separated optical axes of the transmitter and receiver channel. For large angular coverage in the bi-static design the axes of the two channels need to be moved simultaneously. In the mono-static design, on the other hand, a movable mirror which cover the aperture of the transmitter and receiver can be employed for large angular movements. The mono-static design also offers a more compact optical solution compared to the bi-static. Stray-light rejection is an important issue in a system with the optical receiver and transmitter axes co-aligned. Considering a retromodulating communication system a considerable amount of the straylight can be eliminated by using an electronic high-pass band filter in the optical receiver since cw irradiation is used by the interrogating laser.

Several different designs of the optical receiver telescope are possible. The final choice depends on the particular application and the operative range of the communication system. For long-range applications, such as space-based satellite communications, high performance telescopes having large apertures are required. The total weight and volume of the receiver telescope is another issue which needs to be addressed. The system discussed in this report is believed to be used on small platforms (airborne or ground-based) where weight and volume may be critical. Coarse alignment of the receiver telescope can be accomplished with three different principles. A flat mirror (on gimbals) can be used to steer the laser and the receiver field of view to the desired direction in space. An alternative is to place the whole transceiver on a movable gimbal plate. This alternative requires a small system with low mass and volume to reduce the moments of inertia during movements. A more complicated solution is to move the optical telescope and direct the transmit beam along the gimbal axes. The flat mirror configuration has the disadvantage that a relatively large mirror is needed if the receive aperture is large. However, considering a retroreflective free-space optical communication system intended for shorter ranges the aperture is probably less than 10 cm in diameter. Placing the whole system on a movable breadboard have some advantages. Large angular movement can be performed with angular resolution less than 0.1 degrees with a stationary transceiver. The communication system studied in this report is intended to be small and possess low weight so a movable breadboard may provide a solution for large angular coverage. An alternative is a movable out-coupling mirror placed on rotational and goniometer translational stages.

The simplest approach for the receiver telescope is to use a collecting lens (figure 27A) to focus the incident radiation on the detector. The field of view for this simple layout is given by

$$\Omega_r = \frac{d}{f} \tag{4}$$

where d is the detector size and f is the effective focal length of the lens. If an external beam expander, with magnification M, is used to expand the outgoing laser beam the FOV of the receiver is M x Ω_r. Assuming a beam expander with magnification, M = 10x, aperture diameter 10 cm and a focusing lens with $\#/f$ = 2, the FOV varies between 2.9 and 14.3^o for detector size d = 100 and 500 μm, respectively. The simple design shown in figure 27A requires an extra beam expander in a mono-static transceiver which makes this design more bulky compared to the Cassegrain receivers (figure 27B and C). The basic Cassegrain telescope consist of a parabolic primary and hyperbolic secondary mirror which compensate spherical aberrations. Using the Cassegrain design a small and compact optical receiver can be constructed. The secondary mirror can be connected to the telescope body by a frame (figure 27B) or the more robust solution using an optical window (figure 27B). The disadvantage of the Cassegrain design is the higher cost for the aspheric mirrors and the precise mechanical alignment required. The laser beam is coupled out via an elliptical mirror in front of the Cassegrain receiver.

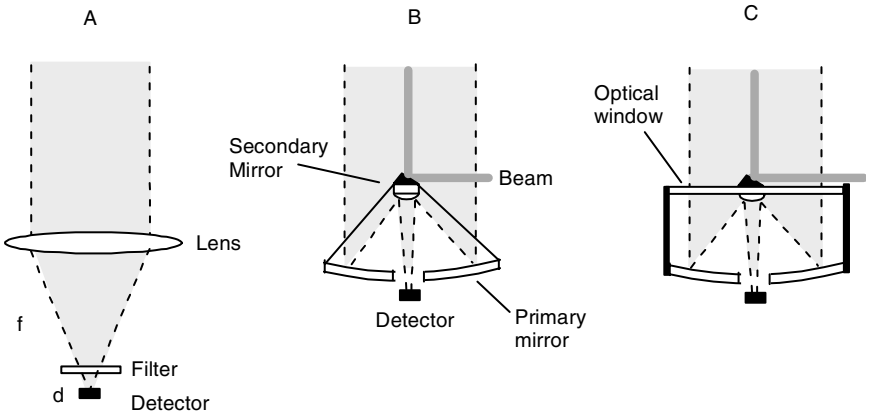

Figure 27. Example of optical receiver telescopes: A) collecting lens. B) and C) telescopes based on the Cassegrain configuration.

A narrow-band optical filter is required to prevent the background radiation to reach the detector and increase the noise contribution. Typically, an interference filter with 10-20 nm linewidth could be employed.

6.1.2.2 Detectors

The most common detector types used in free-space optical communication applications in the wavelength region, λ = 400 to 1100 nm, include PIN or avalanche photodiodes (APD) . Usually the noise equivalent power (NEP) varies from 10^{-12} to 10^{-15} $WHz^{-1/2}$ for these types of photon detectors. The lower value corresponds to “state of the art” detectors. Some characteristic data for these detectors are presented in Table 2. If we assume an optical signal having a bandwidth of 10 MHz the lowest detectable power above the noise limit is tenths of pW. In a retroreflective free-space optical communication system based on intensity modulation of the optical signal a direct detection process is used. Avalanche photodiodes have been widely utilised in free-space optical communication systems. The APD exhibit attracting features such as a low noise contribution and high bandwidth. The internal gain in the APD is usually 50 to 300 times. The response times are in the nano-second region if a small detector surface is used.

Table 2 Typical characteristics for common photodetectors[20]

Parameter/Detector	Si PIN	Si APD	Ge APD
Wavelength [nm]	400 - 1150	400 - 1150	800 - 1750
Quantum efficiency [%]	60 - 90	70 - 80	50 - 80
Gain	1	50 - 300	10 - 100
Dark current [nA]	1	0.1	1 - 50
Detector capacitance [pF]	1 - 5	1 - 5	1 - 5
Response time [ns]	0.3 - 3	0.5 - 5	0.3 - 3
NEP [$WHz^{-1/2}$]	10^{-12}	10^{-15}	10^{-14}

One important issue to consider chosing the detector and preamplifier for a direct detection system is to consider different noise contributions which reduce the sensitivity of the system. Given the noise contribution losses in the communication link attributed to the optical receiver can be estimated. The noise sources can be divided into separate contributions originating from the detector, preamplifier and the background.

6.1.2.3 Optical receiver performance

The signal to noise ratio (SNR) for a detector used in a direct detection optical process can be written as[20]

$$SNR = \frac{(P_s \Re_d)^2}{N_{noise} \cdot B} \tag{5}$$

where P_s is the optical power on the detector, $\Re_d$ is the responsitivity of the detector, B is the receiver bandwidth and N_{noise} is the noise density. For a direct detection optical process all noise contributions can be included in the parameter N_{noise}. As mentioned above the origin of the noise can be attributed to background illumination within the detectors spectral range, intrinsic detector noise (dark current), signal shot-noise and preamplifier noise. Thus, the total noise factor can be summarised as

$$N_{noise}B = i_{bkg}^2 + i_d^2 + i_{ss}^2 + i_{amp}^2 \tag{6}$$

where i_{bkg}^2 is the background contribution, i_d^2 the dark current, i_{ss}^2 the signal shot-noise and i_{amp}^2 the preamplifier contribution, respectively.

The background give rise to DC currents in the detector due to sources such as e.g. sun reflection, ambient light, stray-light in the optical system and celestial sources. The background noise can be written as[1]

$$i_{bkg}^2 = 2qFI_{bkg}B \tag{7}$$

where q is the quantum charge density, I_{bkg} the averaged received background current and B the bandwidth of the receiver. The factor F defines the front-end noise and is defined according to

$$F = Mk_{eff}(1 - k_{eff}) \cdot (2 - M^{-1}). \tag{8}$$

M is the avalanche gain factor and k_{eff} the ionisation coefficient of the photodiode. In the special case of a PIN photodiode is $F = 1$ (due to the internal gain $M = 1$). The background effects enters the average current according to the following expression

$$I_{bkg} = P_{bkg} \cdot \Re_d \tag{9}$$

where P_{bkg} is the collected power arising from the background sources. The background contribution can now be calculated integrating the contribution from the different source over the optical receiver field of view, Ω_{rec}.

$$P_{bkg}^{i} = \int_{A_{rec}} \left(\int_{\Omega_{rec}} H_{bkg}(\Omega)\eta_{rec}B \right) dA \tag{10}$$

In (10) H_{bkg} is the background radiance and η_{rec} is the receiver efficiency. The contribution to the background noise from a single source (denoted i) is determined and the total background contribution is obtained by summarising contributions from all sources.

The dark current in the detector is dependent on intrinsic detector properties. The operating temperature and the size of the detector area give the largest contributions to the dark current. The dark current, and hence, the dark noise can be calculated as

$$i_d^2 = 2qFBI_{dm} + 2qBI_{du} \tag{11}$$

where I_{du} and I_{dm} are the un-multiplied and multiplied dark currents, respectively. Studying the dark current contribution in a PIN photodiode the first term in (11) can be neglected.

The noise contribution from the preamplifier circuitry can be expressed as

$$i_{amp}^2 = \frac{4kTB}{R_f M^2} \tag{12}$$

where R_f is the feedback resistor, k Boltzmann's constant and T the temperature. The major noise contribution from the preamplifier arises from the thermal effects. Since the requirements for high bandwidth and high impedance of the amplifier is difficult to fulfill a transimpedance approach is commonly used for the receiver in optical communication applications[1].

The last term contributing to the total receiver noise in (6) is due to signal shot-noise and defined as

$$i_{ss}^2 = 2qI_{ave}B \tag{13}$$

where I_{ave} is the averaged signal current. The expressions defined above can be used to estimate the total noise contribution from the optical receiver. Moreover, studying eqs. (5) to (13) an understanding of the different noise sources in the detector/pre-amplifier circuitry is obtained.

6.1.2.4 Matching electronics

The signal received from the retromodulator consist of a bit stream where “on/off” keying (OOK) has been used to generate the desired ones or zeros. A schematical layout for the signal conditioning or matching electronics is shown in figure 28. The acquired signal is amplified and conditioned with appropriate filters, passed through an envelope detector, converted to digital format and subsequently fed into a digital signal processor (DSP).

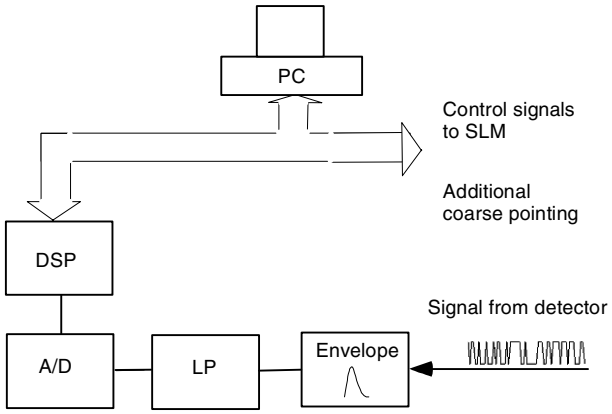

Figure 28. Schematical layout of the matching electronics for conditioning of the acquired bit stream. DSP: signal processor, LP: low pass filter, A/D: analog-to-digital converter, Envelope: envelope detector.

A fast frame grabber card may also be implemented if images are to be captured over the link. The DSP sends control signals to the SLM used for beam steering and handles data from an additional spatial tracker. The spatial tracker may be a quadrant detector or a CCD camera. An alternative to the DSP is to use a FPGA unit if the speed of the DSP limits the highest allowable data rates.

6.1.3 Non-mechanical beam steering

In this section non-mechanical beam steering is considered from the optical and system design point of view. Issues related to principles, performance, strategies etc. have been treated in “Techniques for link establishment and tracking” on page 23.

Several critical parameters limit the optical performance of the non-mechanical beam steerer. In an ideal beam steerer no gaps between the pixels provide efficient modulation of the incident field. The influence of the pixel gaps causes diffraction effects appearing as a static diffraction pattern and responsible for increased optical losses. The complex modulation attributed to the pixel gaps is not easily described since the electrical field may vary significantly over the gap. Thus, a high fill factor of the order of 80 to 90 % reduces the influence of the pixel gaps. The optical transmission through the device is an important parameter since several sources decreases the total optical transmission in the

transceiver. Firstly, nematic and FLC SLM's require polarised light which reduces the optical power from the laser with 50 % (non-polarised laser). Moreover, the losses due to a non-ideal blazed grating may vary between 25 to 50 %. Since these losses may be excessive a relatively high output power from the laser source (~50 mW) is required. An irradiance level of the order of 50 to 100 mW/cm^2 onto the SLM can be anticipated.

Reflective SLM's using nematic LC materials are commercially available and have been investigated for beam steering and shaping puposes[21]. A beam splitter is required to incorporate a reflective SLM into the transceiver (figure 25). The reflective SLM utilises a silicon backplane driver circuit. One problem which arises with reflective type of SLM's is the planarisation of the silicon backplane. A highly non-planar backplane causes unwanted diffraction effects. Transmissive designs have the advantage that no backplane effects are present. If a linear device with a limited number of pixels (e.g. 1x4096) is considered direct addressing should be possible. One requirement for the beam steering device is the necessity to have direct control of all pixels making an adaptive feedback possible. Cross-talk between wanted and unwanted diffraction orders needs to be minimised. Another criteria is that the SLM should not give rise to any additional static wavefront degradations. Preferably, the cover glass of the SLM is AR-coated to reduce first order reflections.

The non-mechanical beam steering device is most likely to be used for micro-scanning and signal optimisation purposes in a retroreflective free-space optical communication system. Methods and principles for beam steering, pointing and tracking have been discussed in "Techniques for link establishment and tracking" on page 23 and ref.[21] Coarse beam steering can be performed using a flat mirror or moving the complete transceiver system. The highest refresh rate of the beam steering device is of the order of 100 Hz using a nematic LC SLM. Since the demonstrator system discussed in this report only consider one-dimensional motion a cylindrical lens can be used to elongate the beam in the vertical directions (retromodulator allowed to be moving along horisontal axis).

6.2 Retromodulator

Two different candidates for the retromodulating receiver are considered. In the corner cube configuration the optical modulator is integrated with a corner cube to provide the reflected optical signal. In the focal plane configuration the modulator is located in a focal plane of a collecting optics or a telescope.

6.2.1 Corner cube configuration

The corner cube configuration of the retromodulator has attractive features since a relative large field of view can be accomplished. The intrinsic properties of a corner cube is to reflect incident light, $\bar{\boldsymbol{k}}$, to the opposite direction, $-\bar{\boldsymbol{k}}$. The two most frequently used methods to obtain this behaviour is to utilise three mutually orthogonal mirrors or a corner cube prism causing total internal reflection at each side. The simplest configuration of a retromodulator is to combine a transmissive MQW modulator with a corner cube retroreflector. Two possible configurations of transmissive and reflective MQW modulators are shown in figure 29. The optical arrangement is simpler using a transmissive component. The divergence of the reflected laser beam from a

retromodulator is to a large extent determined by the diffraction properties of the aperture and the incident optical wave. Discussions about diffraction effects and acceptance angles are presented out in “Numerical wave propagation” on page 52.

High optical quality and mechanical stability is required for the retroreflective corner cube. Misalignment of the mirror surfaces or non-planarity causes a degraded performance. Both the far-field diffraction pattern and the reflections properties are affected. One of the mirrors can be replaced by a reflective MQW modulator. However, this solution requires high accuracy in the alignment and mounting process.

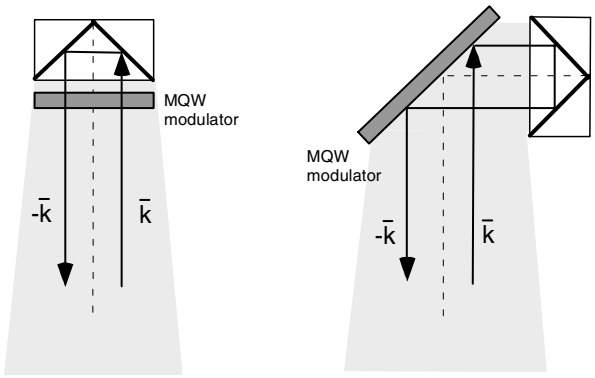

Figure 29. MQW modulator combined with a corner cube retroreflector. Transmissive modulator (left) and reflective modulator (right). **k** depicts the wave vector of the incident light and the shadowed area illustrates the spreading of the reflected beam.

An interesting approach using a corner cube made of glass is to attach a reflective modulator to one side of the cube. However, index matching of the glass-MQW boundary is required in order to couple light into the modulator. One important design parameter of the retromodulator is the acceptance angle of the combined corner cube/MQW modulator.

The acceptance angle and the reflected intensity of various corner cube shapes have been studied[22]. Usually, the operating FOV varies between $\pm 20^{o}$ and $\pm 15^{o}$ for triangular and circular retroreflector configurations, respectively. An example illustrating the variations of the effective reflective area as a function of the angle of incident is shown in figure 30. The effective FOV of the retromodulating receiver can be increased by using an array of single MQW retromodulators. If the retromodulators are placed on, e.g., a spherical surface the effective acceptance angle can be increased substantially. An overlap between the instantaneuos FOV of the single modulators is necessary to prevent “dead” angles of the reflected light.

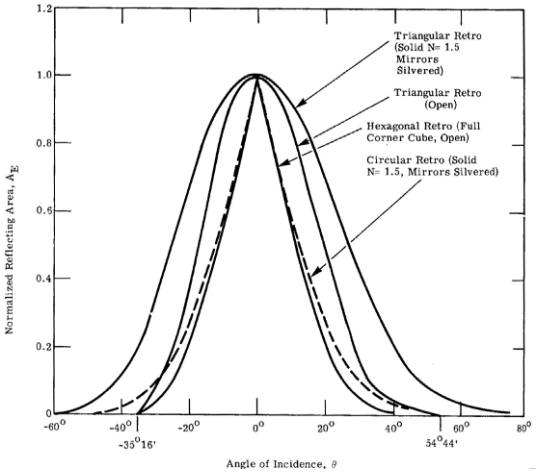

Figure 30. Normalised effective reflecting area of different types of retroreflector configurations as a function of the angle of incidence (from ref.[22]).

The laser cross section for different geometrical shapes of retroreflectors can be calculated. For example, the effective cross-section, σ, of a triangular corner cube is given by

$$\sigma = \frac{4\pi D^2}{3\lambda^2} \tag{14}$$

where D is the aperture diameter. Since the effective retromodulator area can be significant ($\sigma \sim 10^7$ m^2 when D = 1 cm and λ = 850 nm) a large amount of the captured optical power is reflected back to the receiver.

In addition to the MQW modulators/corner cubes the retromodulating receiver may use an extra optical receiver for identification purposes. This extra receiver channel may also be used as a separate communication channel.

6.2.2 Focal plane retroreflector configuration

In the focal plane retroreflector configuration the optical modulator is located in a focal plane of a collecting optics as illustrated in figure 31. The advantage of this configuration, in comparison to the corner cube design, is the possibility to use small optical modulators not limited by the RC time constant. The smallest achievable spot size in a focal plane configuration is defined by the quality of the employed optics. The diffraction limited spot size can be written as

$$w_o = K\frac{\lambda f}{D} \tag{15}$$

where K is a constant of the order of unity describing the incident optical wave ($K = 1.3$ for a Gaussian wave), f the focal length of the lens (or the receiver telescope) and D is the aperture diameter. Aberrations originating from the optical components increase the minimum spot size. One critical parameter for the focal plane retroreflector is the limited field of view. The FOV can be determined using (4).

The effective aperture is larger for the focal plane design. A FOV in the mrad region can be anticipated for normal sized optics (10 cm aperture diameter) and a modulator size of the order 0.1 mm. The focal plane design is best suited for static retromodulator communication links. The narrow FOV put high requirements for the transceiver tracking precision.

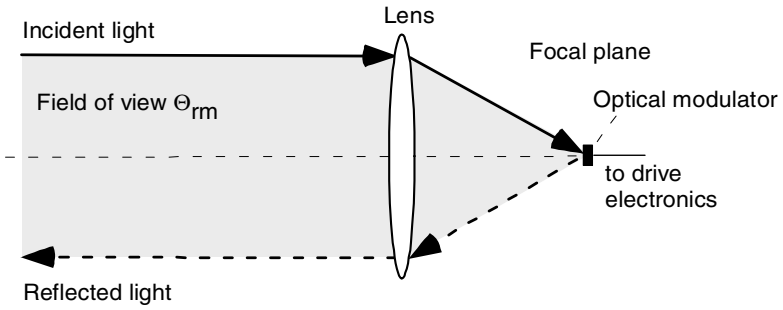

Figure 31. Schematical principle showing retroreflection from a focal plane ("Cat-eye effect").

The received power from a focal plane retroreflecting modulator can be calculated using the laser radar equation

$$P_r = P_t \eta_t \frac{A_\Delta}{\pi(\theta L/2)^2} \frac{A_t}{L^2} \eta_r \eta_{atm} \tag{16}$$

where A_Δ denotes the effective retromodulator area. The other symbols have been defined in "Nomenclature" on page 69. The effective retromodulator area is related to the laser cross-section according to[23]

$$A_\Delta = \frac{\sigma}{4\pi}. \tag{17}$$

The reflection coefficient of the retromodulator decreases the effective cross-section. In summary, the configuration utilising reflection in a focal plane provides a potential for constructing high speed retromodulators but with a limited FOV. The Cassegrain telescope can also be used as receiver in a focal plane arrangement. In comparison to the corner cube configuration described above this solution requires extremely high pointing and tracking performance of the transceiver.

6.3 Search and link establishment

After the coarse alignment of the transceiver unit has occurred a scan (link establishment) process has to take place. In this paragraph the most common scan techniques utilised in free-space communication are reviewed[1],[24]. Different techniques are discussed focusing on the retromodulator application. Two-dimensional scan patterns are discussed in addition to the simple one-dimensional case. Two basic scan principles, spiral and raster scan, are depicted in figure 32. In the spiral scan scheme the spatial coordinates, X_o and Y_o, within the FOV is given by[1]

$$\begin{aligned} X_o &= v_\rho t \cos(v_\varphi t) \\ Y_o &= v_\rho t \sin(v_\varphi t) \end{aligned} \tag{18}$$

where t is the time, v_ρ and v_φ are the radial and angular velocities of the beam, respectively. Assuming a dwell time, T_d, in each point the radial and angular velocities can be calculated as

$$v_\rho = \left(\frac{R_o \frac{\theta}{t}}{2\pi N_\rho T_d} \right)^{\frac{1}{2}} \tag{19}$$

$$v_\varphi = \left(\frac{2\pi N_\rho \theta}{R_o t T_d} \right)^{\frac{1}{2}}$$

N_ρ denotes the number of turns in the spiral, R_o the largest radial distance and θ the beam divergence. The required number of turns can be deduced according to

$$N_\rho = \frac{R_o - \frac{\theta}{2}}{(1-\kappa_\rho)\theta} \tag{20}$$

where κ_ρ is the overlap factor between adjacent turns.

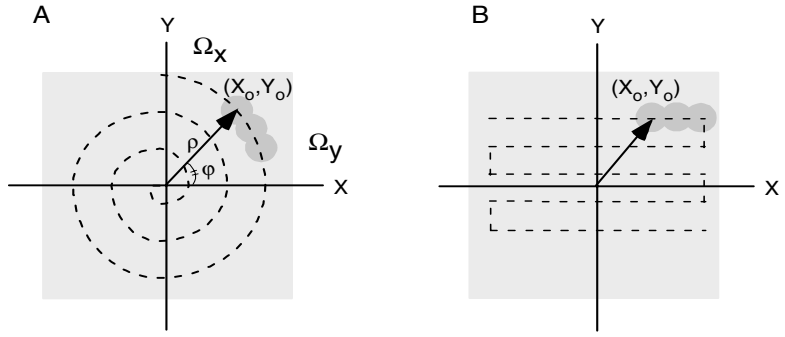

Figure 32. Examples showing a spiral (A) and raster (B) scan principles. The field of view is defined by Ω_x and Ω_y.

The most common scan process is raster scan where a line is scanned for each vertical increment (figure 32B). In the raster process the number of horisontal and vertical scans are defined as[7]

$$N_x \approx \frac{\Omega_y}{\theta(1-\kappa_x)} \tag{21}$$

$$N_y = N_x - 1$$

and κ_x is the overlap between adjacent points. Generally, an overlap between 10 to 20 % is used to overscan the field of view. The total time required to cover the field of view, Ω_x x Ω_y, can be calculated according to

$$T_\Omega^{raster} = \frac{\Omega_x}{v_x}\left(N_x + \frac{\Omega_y}{\Omega_x} + \sqrt{2}\frac{N_x+1}{N_x-1} \right) \tag{22}$$

assuming a constant scan speed v_x and a diagonal re-trace. In the case of a spiral scan process the total scan time can be determined as

$$T_{\Omega}^{spiral} = \frac{2\pi N_{\rho} R_o}{\theta}. \tag{23}$$

In addition, a combination of a spiral and raster scan process could be of interest. After the signal from the retromodulator has been detected a spiral or spiral/raster scan combination can be utilised to optimise the retromodulator signal in a two-dimensional search pattern. Starting the link establishment by searching the complete FOV a threshold could be employed to refine the search in next step by distilling the search area. Alternatively, several thresholds could be used to obtain a successive refinement of the search area aiming to increase the acquisition signal. Using spiral scanning these features are accomplished by reducing ρ and translating the origin of the scan spiral (figure 33).

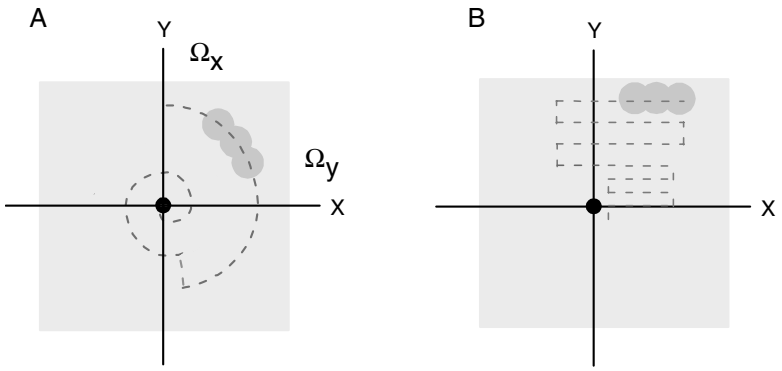

Figure 33. Schematical description of a link establishment using a spiral scan process and successively adopting scan spirals (A). Alternatively, the raster scan can be refined in successive orders (B).

Using SLM's for beam steering phase holograms can be generated which maps the FOV. Since the SLM act as a random access device both spiral and raster scan can be accomplished. The location of the beam within the FOV can be pre-calculated depending on the employed scan scheme.

Limiting the movement of the retromodulator to one-dimension the laser beam is preferably elongated in one direction (e.g. vertical axis) and the link establishment and search process occurs along the horisontal axis. Using a binary FLC SLM one scheme to perform adaptive beam steering was described in "Techniques for link establishment and tracking" on page 23. An example of an 1D scan process is illustrated in figure 34.

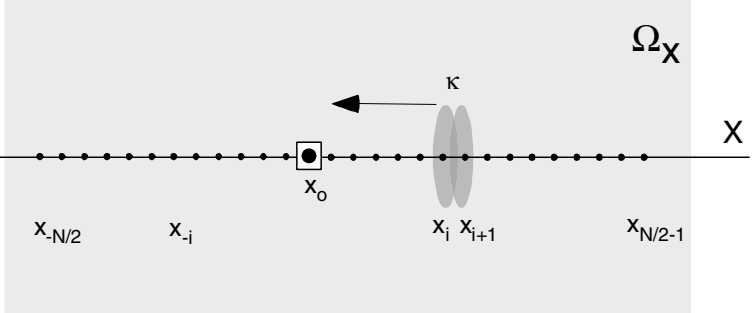

Figure 34. Principle of an 1D scan process to locate a retromodulator. The retromodulator is located at x_o.

The total number of addressable points within the FOV, Ω_x, is equal to N. Depending on the required intensity, cross-talk effects and limitations by the SLM (number of pixels, phase levels, quantisation effects etc.) the number of addressable pixels vary. The size of the scanned FOV is given by $\Omega_x = N\theta_x(1-\kappa)$, where κ is the overlap between adjacent spatial coordinates and θ_x the beam divergence. The time required to scan this FOV can be calculated as

$$T_\Omega \approx \frac{\Omega_x}{\theta_x(1-\kappa)f_o} \tag{24}$$

where f_o is the frame rate of the beam steering device. Here we approximate the dwell time in each point as f_o^{-1}. Assuming that f_o = 150 Hz, θ = 1 mrad, κ = 0.15 and Ω_x varies from 20 to 100 mrad (1.1 to 5.7°) give link establish times of the order of 0.15 and 0.78 s, respectively. An amount of over-scanning is required in order to find the largest signal reflected from the modulator. A simple threshold procedure may be used to refine the scan sequence after the maximum signal has been located. A frame rate of 100-150 Hz is required in order to obtain reasonable scan times for the 1D micro-scanning procedure.

6.4 Tracking system

In general, a two-dimensional spatial pointing and tracking system is needed for a retromodulating free-space optical communication system. Several approaches exist which can be utilised. Tracking and pointing are the most critical functions in satellite communication, so the topic has been extensively studied. The spatial tracking detector can be implemented by introducing a beam splitter along the optical axis in the transceiver (see figure 25). Another alternative is to use the communication detector as a combined receiver/tracker detector. This solution requires, however, a fast read-out capability excluding the integrating CCD device. Two different approaches are of interest considering tracking (fine) in a retromodulating communication system.

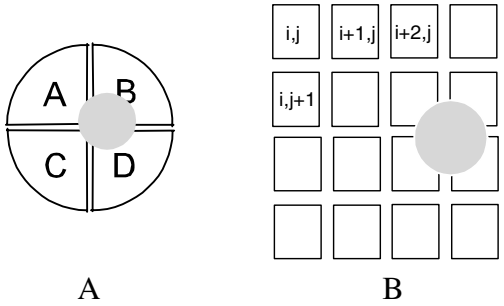

Figure 35. The two most common tracking detectors: quadrant detector (A) and CCD array (B).

The two most common detectors used in spatial tracking are depicted in figure 35. If we use the quadrant detector as an illustrative example the spatial error signals for the tracking process can be calculated as

(25)

$$\bar{x} = \frac{\int_A IdS + \int_C IdS - \left(\int_B IdS + \int_D IdS \right)}{\int_\Sigma IdS}$$

$$\bar{y} = \frac{\int_A IdS + \int_B IdS - \left(\int_C IdS + \int_D IdS \right)}{\int_\Sigma IdS}$$

where I is the intensity, dS denotes the surface of a quadrant and Σ is the total detector area. At short ranges a CCD imaging detector might be favourable for tracking purposes. The retromodulator will act like an optical beacon for tracking in this case. An alternative could be to implement an active light source (LED or semiconductor laser) on the retromodulator. One requirement is a relative high frame rate if fast motion is to be traced. Background noise may interfere with the tracking procedure. Glint reflections from background objects are critical to tracking performance. The reflected communication signal from the retromodulator may also be used for tracking purposes. An envelope detector and a feedback loop to the beam control can be used to optimise the detector signal. Turbulence effects such as, scintillations and beam wander, affect the tracking performance in this case. For coarse tracking the complete transceiver is preferably placed onto a breadboard employing a video camera for tracking. The noise sources affecting the performance of the spatial tracking detector include background effects, dark current, read-out and fixed pattern noise (in the case of an imaging detector).

Considering the retromodulator system discussed in this report only 1D tracking of a moving retromodulator is required. Tracking in one dimension can be accomplished using a position sensitive detector or a linear array detector. A combined communication/tracker detector may be an alternative to a separate tracking channel as mentioned above. The

advantage of using a combined communication/tracking detector is a simpler optical configuration. Cross talk from unwanted diffraction orders may affect the tracking process and should be reduced. In an imaging tracker, for example, unwanted diffraction orders within the transceiver FOV may appear as point sources similar to glint reflections. However, these signals can be identified if the temporal signature can be resolved since they are not modulated. The effective field of view of the retromodulating receiver determine the required accuracy of the tracking process. A wide FOV is accompanied with a large acceptance angle which reduces the constraints on the tracking accuracy. The tracking performance is also affected by noise and turbulence effects which need to be considered when the tracking accuracy is discussed[7].

7 SYSTEM PERFORMANCE AND LINK MODELS

In this paragraph performance models for retromodulating free-space optical communication system are considered. The influence of atmospheric effects upon system performance is studied. Apart from link budget discussions the turbulence influence for double-passage phenomena are reviewed with emphasis on retroreflective free-space communication. Diffraction- and multi-aperture effects are studied using a numerical beam propagation method based on angular spectrum propagation.

7.1 Atmospheric attenuation

The atmospheric attenuation originates from scattering of aerosols and molecular absorption. The total attenuation coefficient, σ_{tot}, describes the accumulated effect during propagation a distance L through the atmosphere. In the case of retromodulation the on-axis peak intensity of the laser beam is reduced by a factor, $e^{-2L\sigma_{tot}}$, due to double-passage through the optical path. The total transmission coefficient for a retromodulating free-space optical communication link was estimated using MODTRAN calculations[25]. Three different weather situations were defined with respect to visibility and rainfall. A sub-arctic summer model atmosphere was assumed to be valid. The propagation path was horisontal and located 5 m above ground. In addition, a slant path (assuming an inclination angle of 30 degrees) was studied. The path length was varied between 1 to 5 km. The parameters used in the calculations are defined in Table 3. Normal gas concentrations (i.e. default to employed model) were used in the calculations.

Table 3 Definition of atmospheric conditions

Atmosphere label	VIS [km]	Rain rate [mm/h]	Clouds	Fog/Aerosols	Comments
A1	23	0	No clouds	No fog/aerosol	Clear sky,
A2	5	0	Nimbostratus	No fog/aerosol	Cloudy sky, reduced visibility
A3	5	5	Nimbistradus	No fog/aerosol	Light rain, bad conditions

VIS = visibility

The MODTRAN calculations show that the transmission window at λ = 850 nm is suitable for free-space optical communication. In good weather situation, i.e. VIS = 23 km, the total transmission for double-passage vary between, 0.81 to 0.36, for ranges up to 5 km.

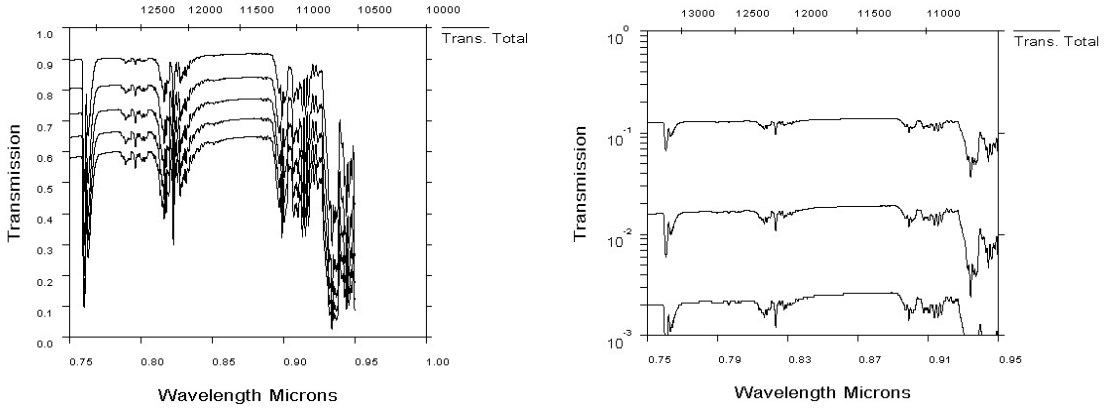

Figure 36. Total transmission through the atmosphere between 1 to 5 km using a horisontal path and assuming a clear sky, model A1 (left). Identical path (1 to 3 km) but in bad weather conditions, model A3 (right).

An example showing atmospheric transmission for single-passage in good and bad weather conditions is depicted in figure 36. The transmission is reduced to 0.01 for double-passage at a distance of 1 km when bad weather conditions (model A3) is experienced. Increasing the range reduces the transmission significantly as observed in figure 36. The total attenuation coefficient was $\sigma_{tot} = 0.1$ km^{-1} at good weather conditions. Degradation of the weather conditions alters the attenuation coefficients to $\sigma_{tot} = 0.43$ and 1.96 km^{-1} for model A2 and A3, respectively. Example of atmospheric transmission values for horisontal and slant paths at λ = 850 nm are presented in Table 4.

As observed in Table 4 the total transmission is significantly reduced at longer ranges when the weather deteriorates. However, at L = 1 km range the transmission vary between $\eta = 0.81$ for clear sky and reduces to $\eta = 0.02$ in rain. The transmission for the slant path is higher due to a reduced extinction along the path at higher altitudes. The purpose of this paragraph was to illustrate how MODTRAN can be used to calculate atmospheric attenuation in a retromodulating free-space optical communication system. More complicated atmospheric models and user defined empirical data can also be implemented in the MODTRAN calculations. In the continuing discussions in this report the atmospheric attenuation was not further stressed and we assume a total attenuation coefficient of σ_{tot} = 0.2 and 2.0 km^{-1}, respectively, to represent clear sky with good visibility and reduced visibility due to rain.

Table 4 Atmospheric transmission ($e^{-2\sigma L}$) calculated by MODTRAN (double-passage)

Path length-L [km]	**A1** Horisontal/slant	**A2** Horisontal/slant	**A3**[1)] Horisontal	**Comments**
1	0.81 / 0.85	0.42 / 0.42	0.02	Distance for demonstrator
2	0.66 / 0.77	0.18 / 0.28	0.4e-3	

Path length-L [km]	**A1** Horisontal/slant	**A2** Horisontal/slant	**A3**[1)] Horisontal	**Comments**
3	0.53 / 0.72	0.07 / 0.25	9.0e-6	
4	0.44 / 0.69	0.03 / 0.23	0.1e-6	
5	0.36 / 0.67	0.01 / 0.22	2.8e-9	

The zenith angle was 30° for the slant path. [1)]Only a horisontal path was considered.

In addition to the MODTRAN models supplementary LZTRAN calculations were carried out bearing in mind that the resolution in MODTRAN is limited studying specific laser lines[26]. However, LZTRAN calculations supported the high transmission window in the 845 to 855 nm wavelength region suggesting that no absorption is expected to occur even if a narrow-band external cavity laser is utilised.

7.2 Analytical link budget model

The link budget, or link margin, can be estimated for a retromodulating free-space optical communication system using the laser radar equation. In this simple treatment turbulence and diffraction effects are neglected. The purpose of using a simplified approach is to obtain a quick estimate of the link budget in a retromodulating free-space optical communication system. The power captured by the optical receiver in the transceiver unit can be calculated as[23]

$$P_r = \left\{ \frac{4P_t}{\pi(\theta_t L)^2} \cdot \eta_t \right\} \times \left\{ \frac{4A_r}{\pi(\theta_r L)^2} \cdot \rho_r \right\} \times \{A_t \eta_t\} \times e^{-2\sigma_{tot} L} \times K \cos\phi \quad . \qquad (26)$$

The first factor in (26) represents the transmitted power, the second factor is attributed to the power reflected by the retromodulator and the third factor is the received optical power. Diffraction effects can be taken into account in an approximative approach by the parameter *K*. The parameters used in (26) are defined in Table 5. The divergence of the interrogating beam was 1 mrad. The signal bandwidth was 10 MHz and an avalanche photodiode (APD) with NEP equal to 10^{-11} $WHz^{-1/2}$ was assumed to be used as detector.

Table 5 Model of a simple retroreflective free-space optical communication link

Symbol	**Parameter**	**Value**
P_t	Laser power	10-100 mW
L	Distance between transmitter and retromodulator	1 km
θ_t	Divergence angle laser	1 mrad
θ_r	Divergence angle retromodulator	50% larger than diffraction limit
A_t	Effective area - receiver	78 cm^2
A_r	Effective area - retromodulator	5 cm^2
ϕ	Angle of incidence	0 degrees
K	Correction factor - diffraction effects	1

Symbol	Parameter	Value
η_r	Total transmission - receiver channel	0.6
η_t	Total transmission - transmitter channel	0.4
ρ_r	Retromodulator - reflectivity	0.3
α	Atmospheric attenuation	0.1 or 2 km^{-1}

Link budget calculations changing the effective retromodulator diameter are depicted in figure 37. Using a narrow beam a large amount of the optical power is reflected back into the transceiver resulting in a link budget above 20 dB for small retromodulator effective area exceeding $A_r > 3$ cm^2. It was assumed that the radiation reflected from the retromodulator had a divergence twice that of the diffraction limit.

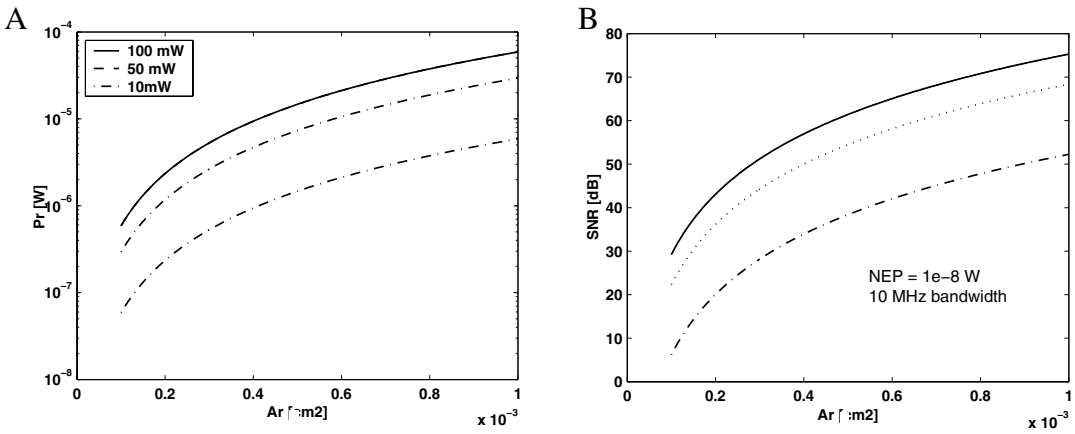

Figure 37. Received power as a function of the effective retromodulator diameter (A). SNR as a function of the effective retromodulator diameter (B).

In order to include turbulence effects in the performance estimations a beam propagation model for the double-passage phenomena was used[27],[28]. Neglecting turbulence, in a first approximation, this model can be used to study the influence of the retromodulator aperture and the properties of an incident Gaussian beam wave. A summary describing the model is given in “Laser beam propagation i double-passage phenomena” on page 64.

Properties like the beam divergence, effective retromodulator area and receiver aperture can be altered. Two different cases were studied using a collimated (diffraction limited) and a divergent (1 mrad) beam. The transmitter beam radius (W_o) was altered between 1 to 2 cm. The beam radius at the retromodulator (W_1) determines whether diffraction effects introduced by the retromodulator aperture govern the size of the reflected beam. In figure 38A, is the beam radius in the transceiver plane plotted versus the retromodulator radius (W_R) for a collimated beam using different transmitter apertures. A minimum exist when W_R is slightly larger than the beam radius at the transmitter, W_o. If $W_o << W_R$, Gaussian beam propagation effects dominates while, $W_o >> W_R$, results in diffraction governed by the shape and size of the aperture. A collimated beam give rise to a narrow

beam profile at range, L = 1 km, making tracking and pointing issues critical. The reflected optical intensity captured by the optical receiver is high. Note, a central obscuration in a Cassegrain receiver may partly block the reflected light.

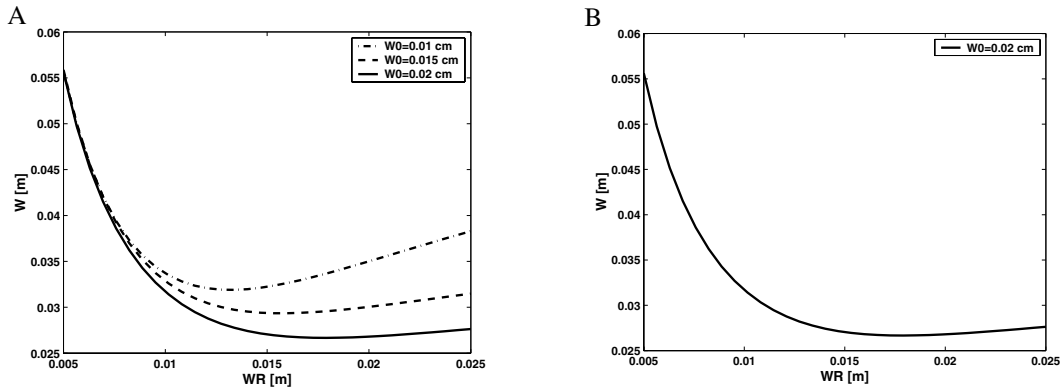

Figure 38. A) Calculated beam radius in the transceiver plane (W) as a function of the effective retromodulator (W_R) radius assuming a collimated beam. B) Same as A) but using a beam with 1 mrad divergence. The wavelength was λ = 850 nm.

Increasing the beam divergence at the transceiver causes the reflected beam divergence to decrease compared to the collimated case (figure 38 B). The divergence of the reflected beam can be estimated as

$$\theta = 1.22\frac{\lambda}{W_R} \tag{27}$$

assuming that the incident beam can be approximated with a plane wave.

In the case of a collimated transmitter beam is the relative power captured by the optical receiver relative high at L = 1 km range as depicted in figure 39 A. If the beam radius is increased to W_o = 1 cm the captured power increases by factor five due to the lower divergence. The radius of the beam at the retromodulator (collimated beam) is W_1 = 2.8 cm for a transmitter aperture having 1 cm radius. Hence, very accurate tracking is require for the collimated beam case.

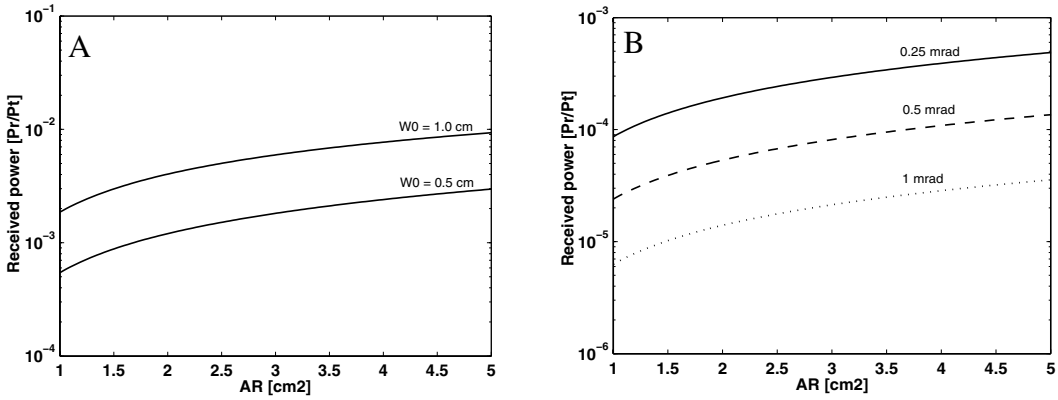

Figure 39. A) Calculated relative intensity as a function of the effective retromodulator (A_R) area assuming a collimated beam. B) Same as A) but using a beam with 0.25, 0.5 and 1 mrad divergence. The wavelength was λ = 850 nm.

In figure 39 B, the transmitter beam divergence was varied as a function of the effective retromodulator area. The relative captured power in the optical receiver decreased approximately one order in magnitude if the beam divergence was increased from 0.25 to 1 mrad. Depending on the required pointing accuracy a captured power above the NEP can be easily obtained even for small retromodulator dimensions. For example, assuming a pointing error of 100 μrad (1 mrad beam divergence) the on-axis intensity in the plane of the retromodulator is only altered 8 %. Using the numerical model effects on the captured power due to pointing errors can be studied.

7.3 Turbulence effects

Several turbulence effects need to be considered studying the performance of a free-space optical communication system. Atmospheric turbulence can degrade the performance considerably by introducing bit errors or longer periods of signal drop-out (fading). The most important phenomena include:

- Transversal intensity variations (scintillations)
- Beam spreading
- Beam wandering
- Angle-of-arrival fluctuations
- Enhanced backscatter effects (double-passage phenomena).

Beam spreading increases the effective beam radius at the retromodulator and consequently the intensity in the reflected signal is reduced. In the treatment in this report we assume that angle of arrival fluctuations can be neglected in relation to the magnitude of the intensity scintillations and beam wandering. Scintillations i.e. spatially variations in the beam intensity due to turbulence causes fading and signal drop-outs. These effects can be serious for the performance of the communication link if the turbulence is strong. The time scale for the scintillations are usually of the order of 1 to 10 ms depending on the turbulence strength. Beam wander occurs on a slower time scale and can be described as a stochastic movement of the beam centroid over the retromodulator and receiver aperture. One important feature of retroreflective free-space optical communication is the double-passage beam propagation (c.f. laser radar) meaning that turbulence effect need to be calculated taking this into account. One attribute of the double-passage is enhanced backscatter whereas incident and reflected beam can be correlated due to turbulence resulting in increased on-axis peak intensity and increased off-axis variations in the receiver plane[29]. The background for turbulence effects in double-passage situations are reviewed in appendix *"A1.2 Turbulence effects"*. Link parameters defined in Table 5 were used throughout the calculations presented in this paragraph. Turbulence parameters are specified for each separate case.

The point target approximation is assumed, i.e. $\Omega_R >> 1$ which is reasonable for a divergent beam. The correlation term between the forward and reflected wave determines the magnitude of the enhanced backscatter effect. The effect is most noticeable on-axis and can be neglected considering off-axis effects.

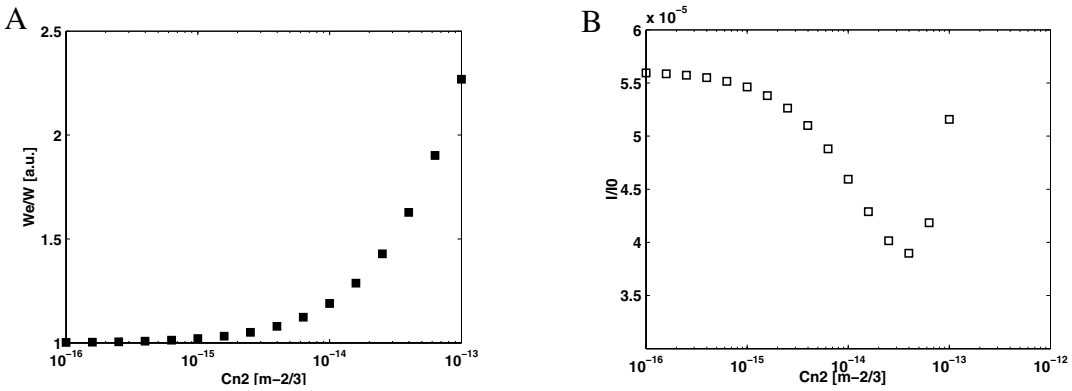

Figure 40. A) Relative beam radius at the transceiver as a function of the turbulence strength. B) Relative on-axis intensity as a function of the turbulence strength. The parameters were the same as above i.e. 1 mrad beam divergence, W_o = 1 cm, W_R = 1.26 cm (effective area 5 cm^2) and L = 1 km.

Turbulence broadening of the beam radius is most evident at turbulence strengths above $C_n^2 > 10^{-14}$ $m^{-2/3}$ (figure 40). In strong turbulence conditions the relative broadening of the effective beam radius (W_e/W) at the transceiver is approximately a factor two. In these calculation effects due to enhanced backscatter was included. If we now consider the relative on-axis intensity variations as a function of the structure parameter, C_n^2, the on-axis decreases in presence of weak turbulence (figure 40B). The enhance backscatter contribution can be omitted in this region. At moderate turbulence strength ($C_n^2 > 10^{-14}$) $m^{-2/3}$ the enhanced backscatter term and the relative on-axis ratio increases. Since this effect is only observed close to the optical axis the intensity was calculated as a function of the radial coordinate and integrated over the optical receiver aperture to obtain the captured power by the transceiver.

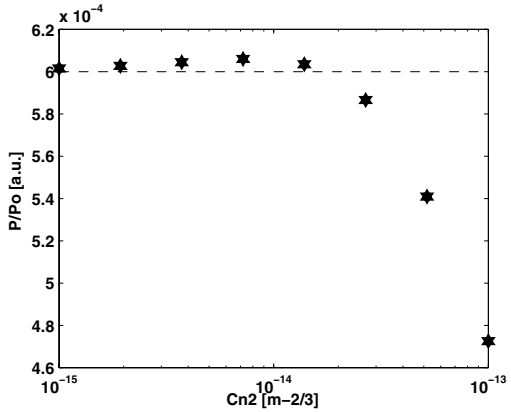

Figure 41. Calculated captured power (10 cm receiver aperture diameter) as a function of the turbulence strength. The transmitter and retroreflector parameters were; W_o = 1 cm, F_o = -20 m and W_R = 1.3 cm.

In figure 41 is the captured power plotted versus the turbulence strength assuming a collecting aperture with 10 cm diameter. The star denotes the integrated power collected by the aperture including both beam broadening and enhanced backscatter. The contribution from turbulence is rather small and may be neglected in presence of weak or moderate turbulence. The reduction in average power can be compensated by increasing the laser power in the transceiver.

The fade statistics, or probability of signal fading, can be calculated using the expressions derived in *"A1.2 Turbulence effects"*. The fade probability is expressed as a function of the fade level, F_t, describing the signal strength above the detection threshold. The fade probability varies strongly depending on the turbulence level as observed in figure 42.

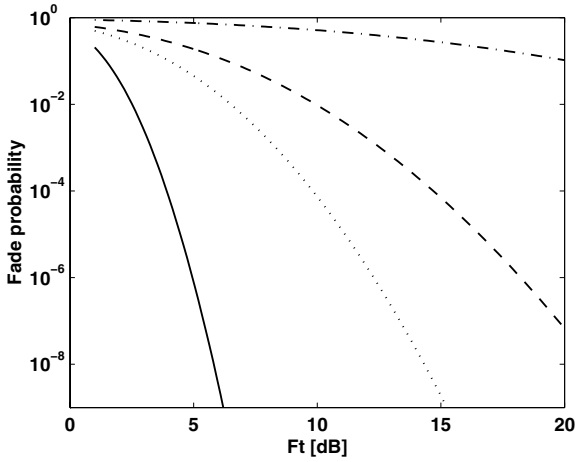

Figure 42. Fade probability as a function of the fade threshold, F_t, for turbulence level $C_n^2 = 1x10^{-15}$ (solid), $5x10^{-14}$ (dotted), $1x10^{-14}$ (dash), $5x10^{-13}$ (dash-dotted) $m^{-2/3}$.

At relative strong turbulence conditions the fade probability remains high although $F_t >$ 10 dB. Weak turbulence gives a fade probability < 10^{-8} for fade levels F_t of the order of 5 dB or larger. These results indicate that turbulence effects may cause serious fading events if the turbulence is strong. In these cases it might be neccessary to try to compensate for the turbulence effects by using multiple apertures or increasing the single aperture diameter.

Other important properties are the fade frequency and the fade time, both affecting the bit error rate of an optical communication system. The fade frequency is defined according to eq. (A16) in appendix *"A1.2 Turbulence effects"*. Recent studies of free-space optical communication through atmospheric channels where moderate to strong turbulence is present have suggested that a gamma-gamma distribution function should be used to describe the scintillation properties. It should be of interest to include the gamma-gamma distribution function describing a double-passage situation. The expressions for the fade probablity, frequency and fade time need to be recalculated in this case. Future studies focusing on fade statistics should include these types of calculations for a double-passage case.

7.4 Numerical wave propagation

In order to study diffraction effects due to the retromodulator geometry numerical beam propagation calculations were performed. The objective was to extract information about the diffraction effects from single- and multiple apertures in the far-field.

One way to describe propagation of an optical field is to use scalar Fresnel diffraction theory and the angular spectrum propagation method. The optical field can be expressed by $u = u(\bar{r}, t)$, where u is a complex valued function, depending both on the spatial variable $\bar{r}$ and time. In the discussion below the time dependence of the field is neglected. In this representation we can express a Gaussian beam wave as

(28)

$$u(r,z) = e^{-i\left(\frac{r}{w(z)}\right)^2} \cdot e^{-i\frac{kr^2}{R(z)}}$$

where *w(z)* is the beam radius, *R(z)* the phase radius, *r* the radial coordinate and *k* the wave vector. The optical field may be expressed as a summation of the spatial frequency components (or the inverse Fourier transform of its frequency content)

(29)

$$u(x,y) = \int_{-\infty}^{\infty}\int_{-\infty}^{\infty} U(\xi,\eta)\cdot e^{j2\pi(x\xi+y\eta)}d\xi d\eta$$

where ξ and η define spatial frequency variables. In the Fresnel approximation (operator notation) the propagation of the field u in free space from z = 0 to L can be written as

. (30)

$$u(x,y,L) = \boldsymbol{F}^{-1}\{H_f \boldsymbol{F}\{u(x,y,0)\}\}$$

$\boldsymbol{F}$ and $\boldsymbol{F}^{-1}$ denote the spatial Fourier and inverse Fourier transforms, respectively. The Fresnel propagation operator valid in the near- and far field regions, H_f, is defined as

(31)

$$H_f = e^{jkL}e^{-j\pi\lambda d(\xi^2+\eta^2)}$$

Using (30) for free-space propagation care need to be taken at longer propagation distances to avoid problems due to aliasing. This method of beam propagation is also known as angular spectrum propagation. The models used in this report were contructed using a commercial code for angular spectrum propagation[30].

7.4.1 Single and multiple-apertures

In this model similar parameters as those presented in vacuum propagation case were utilised. The beam divergence was 1 mrad obtained by setting the initial phase radius to F_o = -20 m. The divergence was kept constant throughout all calcutions discussed in this paragraph. Taking the size of the retromodulator apertures and the radius of the wavefront in front of the retromodulator into consideration the incident beam on the retromodulator can be approximated with a plane wave. Hence, characteristics of plane wave diffraction patterns can be expected in the transceiver plane.

In the single aperture case the square and circular apertures correspond to sinc and Bessel intensity distributions, respectively[31]. An example showing calculated intensity distributions at the transceiver plane is depicted in figure 43.

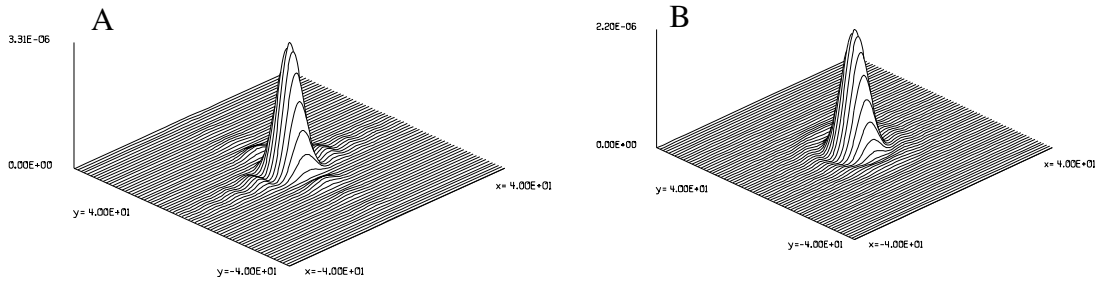

Figure 43. A) Far-field intensity distribution from a single square aperture (1x1 cm^2) in the transceiver plane (L = 1 km). B) Same as A) but circular aperture.Units on x- and y-axis are in cm.

Only the shape of the multiple-aperture and the distance between sub-apertures affect the far-field intensity pattern. Two model apertures are shown in figure 44. The purpose of the models was to study diffraction and interference effects in the far-field. Two extreme cases can be imagined; if the distance between the sub-apertures is large the apertures can be considered as isolated sources giving rise to separate sinc distributions (rectangular array) in the transceiver plane. The other case is obtained by removing the gap between the sub-apertures and the far-field pattern can be treated as the response from a single generally shaped aperture. Between the two extreme situations a complicated interference pattern which depends on the shape of sub-apertures, number of apertures and distance between the apertures can be observed.

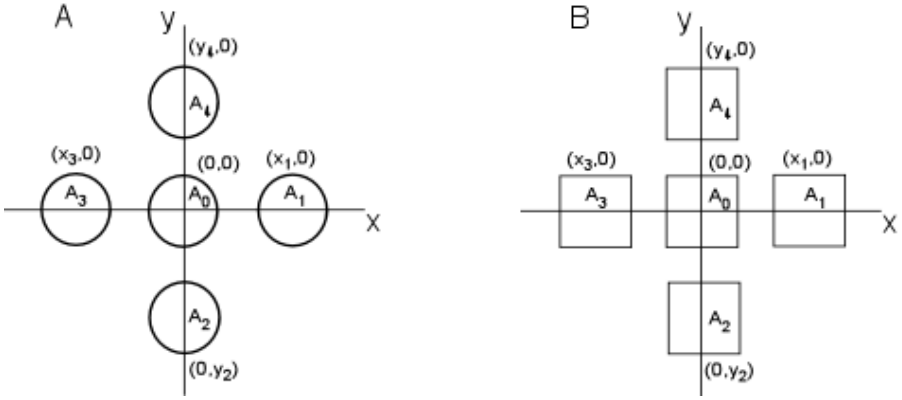

Figure 44. Example of the retromodulator geometries utilised in the physical optics calculcations. Circular (A) and quadratic (B) retromodulator apertures.

The effect of increasing the distance between quadratic multiple-apertures (1x1 cm^2 area) is illustrated in figure 45. Increasing the distance from 2.5 to 5.0 cm causes a gradual broadening of the intensity observed in the transceiver plane. The interference effects are also significantly reduced. Further increase of the distance results in a far-field intensity distribution which can be considered as five separate contributions from single quadratic apertures. I this case each intensity distribution resembles a sinc-function. The effect of the optical receiver is to collect the power within a given aperture. A brodening of the intensity distribution, hence, causes a reduced signal. The beam divergence also effects the behaviour in the transceiver plane. In the example presented above a divergent beam (1mrad) was considered. If the beam divergence is reduced (in order to increase the reflected intensity) a larger part of the reflected irradiation is captured by the reciever

optics. A reduction of the beam divergence also causes a varying intensity distribution reflected from the different sub-apertures. The major contribution originates from the central aperture in the case of a diffraction limited beam.

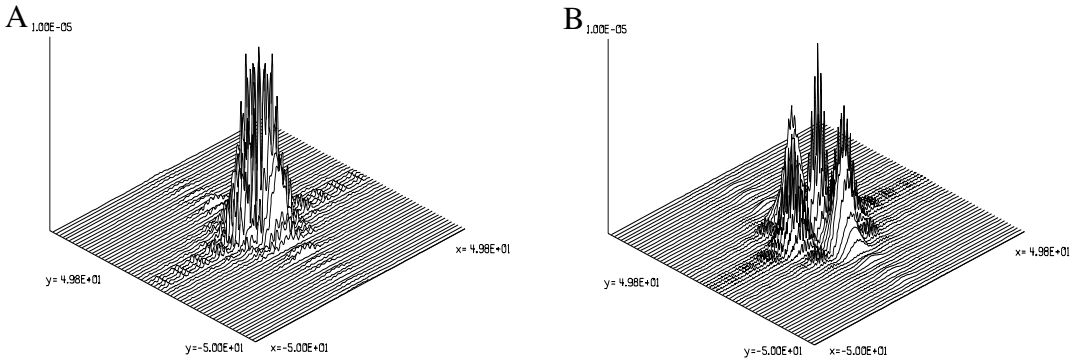

Figure 45. Example showing the effects on intensity of an increased distance between individual apertures (reflection from quadratic multi-aperture). The equidistance was 2.5 cm (A) and 5.0 cm (B).

Separation of the distance between the individual apertures causes a decrease of the captured power. For example, an increase of the distance from 2.5 to 5.0 cm (for a quadratic array and W_R = 0.5 cm) reduces the captured power approximately 50 %. In figure 46 is the reduction in the captured power depicted as a function of the aperture distance. The model described in this paragraph can be used to optimise the distance between the apertures. Important parameters affecting the captured power include: shape and size of apertures, distance between the apertures and the dimension of the receiver optics.

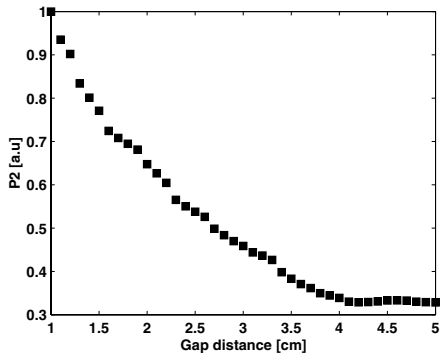

Figure 46. Reduction of the captured power in the transceiver plane as function of the aperture distance. The following parameters were used: beam parameters as above (1mrad), W_R = 0.5 cm and quadratic aperture.

7.4.2 Focal plane reflections

Using the physical optics model a simple focal plane retromodulator configuration can be analysed. The model consist of a simple collecting lens (W_R = 2.5 cm) and a mirror representing the retromodulator. The angle of incident was altered and diffraction effects could be studied within and at the FOV edges. Only diffraction effects were treated in the model i.e. no blurring of the focused beam due to aberrations in the collecting lens was included. However, aberrations due to non-perfect optics can easily be implemented by adding a degraded wavefront describing the aberrations. An example showing how the captured power in the transceiver plane varies as a function of the angle of incidence is

depicted in figure 47. The captured intensity vanish outside the FOV. Since the spot size was diffraction limited in this example the decrease in intensity occurs abrupt at the FOV border. Inclusion of aberrations due to optical components or atmospheric effects increase the spot size, hence, reducing the steepness of this border. The size of the FOV is considerable smaller than the retromodulating receiver configuration utilising corner cube reflectors.

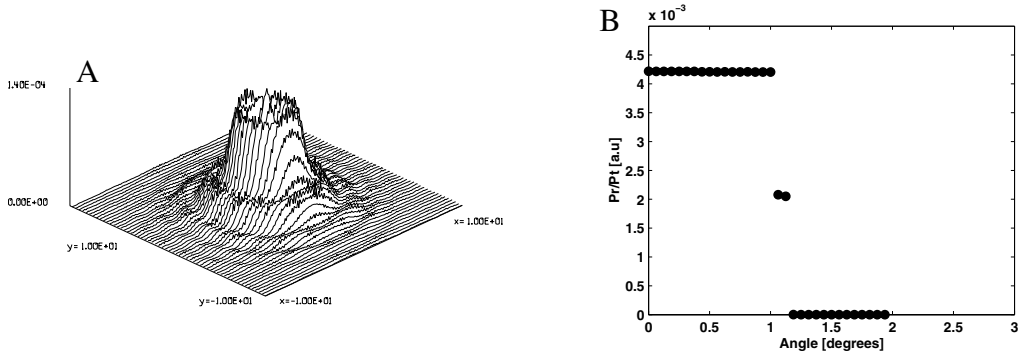

Figure 47. Focal plane reflection communication system. A) Beam profile at transceiver. B) Captured power in the transceiver plane as a function of the angle of incident.

7.4.3 Turbulence effects

Turbulence effects can be included in the numerical model by using the method of phase screens. The turbulence model employed has previously been described and assumes weak turbulence conditions[32]. The model is based on a modified Kolmogorov spectrum and it has been shown that the Rytov theory for the intensity scintillations was satified by the model. The model was also able to predict the phenomenon of saturation. Successive phase screens (with a typical separation of $\Delta z = 100$ m) are used to represent the wavefront aberrations generated by turbulence. Using this method spatial intensity variations in the transceiver plane can be calculated. Hence, effects of different receiver geometries in combination with turbulence effects can be studied. An appropriate treatment of the atmospheric turbulence suggest utilisation of the "frozen spectrum" hyphothesis, meaning that the turbulence spectrum does not alter during propagation in the forward and backward direction.

In order to illustrate how the model can be used for estimation of turbulence effects in a retromodulating free-space optical communication system the square array of retroreflectors described above was studied. In figure 48 the irradiance profile before is striking the reflector array depicted for different levels of turbulence. The intensity variations are considerbly increased when the strength of the turbulence changes from $C_n^2 = 10^{-15}$ to 10^{-13} $m^{-2/3}$. It should be emphasised that several realisations of the calculations are required in order to take statistical effects into account since each phase screen is generated randomly following the Kolmogorov spectrum. The results showed in this paragraph only indicate how this model can be used to study the influence of turbulence in a retromodulating communication system. An improved model should take effects of enhanced backscatter into account.

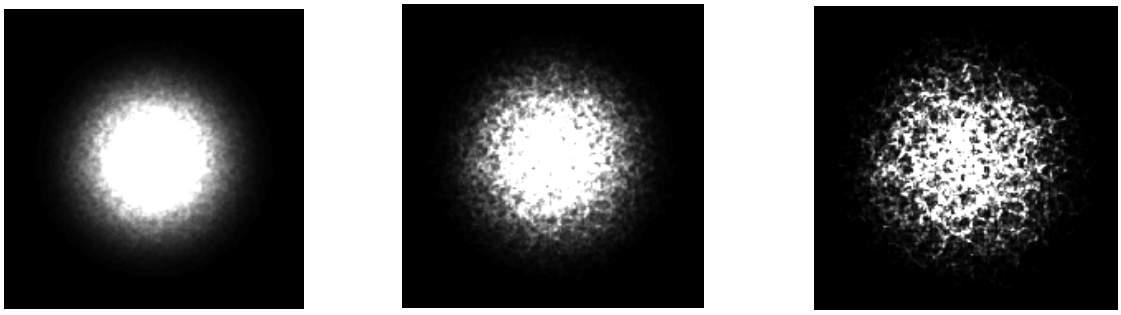

Figure 48. Example showing scintillations as a function of turbulence strength using $C_n^2 = 10^{-15}$, 10^{-14} and 10^{-13} $m^{-2/3}$ (from left to right). Beam profiles before reflection at the retromodulator are shown. The distance was L = 1000 m and λ = 850 nm. A divergent beam was used (1 mrad divergence).

One important issue is to obtain information about fading properties due to turbulence effects. The effect of fading is illustrated in figure 49. In this example we used the square array described above and an optical receiver with an aperture radius W_2 = 5 cm. If the turbulence is increased from, $C_n^2 = 10^{-15}$ to 10^{-13} $m^{-2/3}$, the intensity fluctuation increases dramatically. The magnitude of the intensity variations could be almost two order in magnitude according to the calculations. At the weaker turbulence strenght the variations are more modest as shown in figure 49 A. Several parameters affect the fading properties. Fading effects can be reduced by using multiple apertures in free-space optical communication.

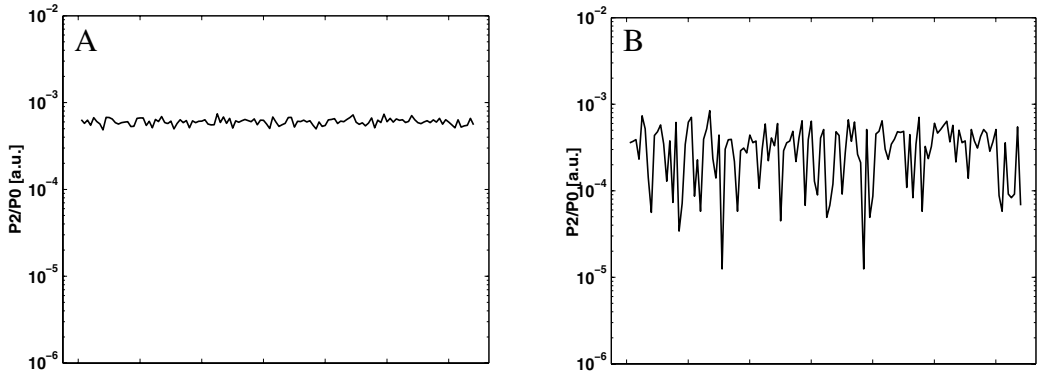

Figure 49. Calculated irradiance fluctations using a optical receiver with an aperture radius W_2 = 5 cm at different turbulence strenghs. A) $C_n^2 = 10^{-15}$ $m^{-2/3}$ and B) $C_n^2 = 10^{-13}$ $m^{-2/3}$.

8 DISCUSSION AND CONCLUSIONS

The purpose of this report was to review technologies and principles for a free-space optical communication system using retroreflection and modulation of the reflected radiation for information transfer. The performance of a retromodulation optical communication system depends on several factors involving e.g. component limitations, system configuration and atmospheric effects. Parameters limiting the system

performance have been identified and discussed. Two basic functions have been emphasised involving non-mechanical laser beam steering using SLM technology and a retromodulator based on multiple quantum wells. A suite of performance models have been described. These models will be be used in a system definition phase.

Several applications have been identified and discussed in this report. The most important features of a retromodulating free-space optical communication system is the possibility to manufacture a technical simple retromodulator with small weight and volume, consumes a limited amount of power and permits relatively high data transfer rates. These features make the concept attracting for small airborne applications involving, for example, un-manned aerial vehicles. The use of large acceptance angles for the retromodulator reduces the tracking and pointing requirements on the transceiver unit. Traditionally, the tracking and pointing assembly contributes to a major part of the total cost in a free-space optical communication system. Non-mechanical laser beam steering shows promising features to be used with narrow FOV and high pointing precision. Although, the SLM's available today do not fulfill all the requirements for implementation as beam steering and beam forming devices, no fundamental limitations exist preventing these components to be employed in future applications.

In this section results presented in the literature covering principles of retro-reflection and free-space optical communication are reviewed. Ferroelectric LC optical modulators have been used in a retrocommunication experiment for free-space optical communication[6]. The retromodulator was attached to a balloon and a ground-based laser transmitter was used for interrogation. It was shown that data transfer rates up to 20 kbit/s could be obtained. Fast large area MQW modulators have been studied for laser communication[3]-[5]. Using MQW modulators data transfer rates between 4 to 6 Mbit/s were obtained using transmissive and reflective MQW modulators. In a recent study communication to an UAV was studied[3]. The bit error rate was reported to be less than 10^{-6} for a short distance indoor link. Coherent free-space optical communication system using piezoelectric retromodulator has been studied[33]. Transfer of an audio signal using a CO_2 coherent laser system over 24 km was described. Small silicon based mechanical retro-reflectors (1x1x1 mm^3) are studied for free-space optical communication[34]. A central transceiver unit is used to interrogate several miniature retroreflectors sending information at approximately 1 to 5 kbit/s.

A large part of the content in the present report covered system related issues. Both corner cube and focal plane retromodulator receivers were discussed. A corner cube retromodulator has the advantages that the acceptance angle can be rather large. The focal plane retromodulator, on the other hand, has a very narrow field of view but allows for small modulator dimensions with short response times increasing the maximum data transfer rates of the communication link. The small FOV of the focal plane retromodulator makes it more appropriate for applications involving a static receiver configuration. As an effect of the small FOV high precision and tracking accuracy is required. For the demonstrator system primarly studied in this report a moving (1D) retromodulator receiver is considered. The large acceptance angle of the corner cube retromodulator configuration makes it the primary candidate for the demonstration. An acceptance angle of $\pm 10 - 15^{o}$ is considered to be suitable for the retromodulator.

As pointed out above coarse beam steering over a wide FOV is preferably peformed by a video tracking system where the transceiver unit is placed on a movable breadboard. Using the glint reflection from the retromodulator coarse pointing and tracking can be performed. The fine tracking and signal optimisation is carried out using the LC SLM. In the present study beam steering was discussed using experimental results from FLC SLM's. Reflective FLC and NLC SLM's mounted on silicon drive circuits are commercially available. The NLC SLM's have the advantage that higher beam steering efficiency can be obtained due to the analog phase response. However, the response time is limited and usually the SLM can not be updated, from a practical point of view, with a higher rate than 25 to 50 Hz. The FLC SLM, on the other hand, provides a faster time response but the steering efficiency is limited due to the binary nature of the FLC material. Different transceiver configurations were discussed in the previous paragraphs. The monostatic configuration is considered to be most appropriate for a system including the beam steering features discussed in this report.

One critical component in the retroreflective optical communication system is the MQW modulator. Important parameters affecting the performance of the communication system include: response time, contrast ratio and acceptance angle. The response time should be less than 0.1 μs to fulfill the objectives of the demonstrator system. The response time is limited by the RC constant of the modulator and the corresponding trans-impedence preamplifier. A contrast ratio of the order of 1:5-10 is required for the reflective MQW modulator to obtain a satisfactory signal to noise ratio. The contrast ratio affects the modulation depth of the reflected signal. The acceptance angle of the reflective MQW modulator and the retroreflector should approximately match each other for optimal FOV. One complication which arises if a Fabry-Pérot cavity design is used to optimise the contrast ratio is the angular dependence of the reflectivity.

Several models have been explored in this report which can be used to calculate the performance of a retroreflective free-space optical communication system. A quick estimate of the technical requirements was made using analytical expressions. An effective retromodulator area of approximately 5 cm^2, 10 - 50 mW laser power and 1 mrad beam divergence results in link budgets above 20 dB (assuming good visibility). MODTRAN calculations indicate hight transmission at λ = 845-855 nm, if the weather conditions are good. Bad weather conditions may decrease the atmospheric transmission two to three order in magntitude for 1 km distance between the transceiver and the retromodulator. In addition to the analytical link budget model theoretical models can be utilised to estimate the effects orginating from atmospheric turbulence.

Characteristic for a retromodulating communication system are effects attributed to double-passage configurations. The effects from enhanced backscatter can be neglected if a relative large collecting aperture is employed by the optical receiver. Although increased on-axis intensity can be obtained these effects are negligable considering the off-axis contribution. Scintillations or transversal intensity variations in the beam profile cause signal drop-outs (fading) of the received signal. According to numerical calculations performed in this study the signal magnitude can vary approximately two order in magnitude in presence of relative strong turbulence. One disadvantage with the numerical calculations is that the temporal variation of the signal is not included. In order to study fade statistics for double-passage phenomena and strong turbulence situations different probability distribution functions need to be considered. Work is in progress

comparing the lognormal and gamma-gamma distribution function for estimating fade statistics in a double-passage optical communication systems. The numerical model based on angular spectrum propagation can be utilised to optimise the number of individual MQW modulators and the configuration of the retromodulator array. Employment of an array of MQW modulators reduce the influence of the scintillations. The individual MQW modulators can be considered as separate transmitter apertures. Hence, the reduction of the scintillation effects depends both on the turbulence strength and the individual locations of the apertures in the retromodulator plane.

In conclusion, this report provides a system description of a retroreflective free-space optical communication system and models for calculating performance. Individual sub-components and functions have been described. The content in this work can be used as a basis for the system definition study. Performance calculations show that a satisfactory link budget can be accomplished for the demonstrator system in presence of good weather conditions. Further work on fade statistics and the turbulence influence for a retromodulating free-space optical communication system is proposed.

9 REFERENCES

[1] S. G. Lambert and W. L. Casey, *Laser Communications in Space*, Artech House, NewYork, 1995.

[2] G. C. Gilbreath, W. S. Rabinovich, and M. J. Montes, “Large-aperture multiple quantum well modulating retroreflector for free-space optical data transfer on unmanned aerial vehicles”, *Opt. Eng*., vol. 40, pp. 1348-1356, 2001.

[3] G. C. Gilbreath, W. S. Rabinovich, T. J. Meehan, M. J.Vilcheck, R. Mahon, R. Burris, M. Ferraro, I. Sokolsky, J. A. Vasquez, C. S. Bovais, K. Cochrell, K. C. Goins, R.Barbehenn, D. S. Katzer, K. Ikossi-Anastasiou and M. J. Montes, "Compact, Lightweight Payload for Covert Data Link using a Multiple Quantum Well Modulating Retro-reflector on a Small Rotary-Wing Unmanned Airborne Vehicle", *Proc. SPIE*, vol. 4127, pp. 57-67, 2001.

[4] G.C. Gilbreath, W.S. Rabinovich, R. Mahon, M. R. Corson, M. Ferraro, D. S. Katzer, K. Ikossi-Anastasiou, T. J. Meehan, and J. F. Kline, "Large Aperture Multiple Quantum Well Shutters for Fast Retroreflected Optical Data Links in Free Space", *Proc. SPIE*, vol. 3707, pp. 666-672, 1998.

[5] G. Charmaine Gilbreath, W. S. Rabinovich, and M. J. Vilcheck, ”Modulating Retroreflector Architecture using Multiple Quantum Wells for Free Space Communications”, *Proc. SPIE*, vol. 3491, pp. 581-586, 1998.

[6] C.M. Swenson och C.A. Steed, ”Low power FLC-based retromodulator communication system”, *SPIE*, vol. 2990, pp. 296-310, 1997.

[7] S. Hård, S. Jacobsson, B. Löfving, U. Olin, P. Rudquist, L. Sjöqvist, O. Steinvall and S. Walles, “Laser Beam Steering - An Introductory Study”, FOA Report, ISSN 1104-9154, FOA-R--99-01158-408--SE, 1999.

[8] R. Andrews, L. Phillips and C. Hopen, *Laser Beam Scintillation with Applications,* SPIE Press, vol. PM99, Bellignham, Washington, 2001.

[9] Efron Uzi., and Livescu G., “ Multiple Quantum Well Spatial Light Modulators ”, in *Spatial Light Modulator Technology*: Materials, Devices, and Applications, Efron Uzi, ed., Marcel Dekker pp. 217-230, 1995.

[10] L. Sjöqvist, K. D’ havé, S. Hård, T. Matuszczyk, P. Rudquist and S. Walles, “Laser beam steering - Final report”, FOA Report, ISSN 1104-9154, FOA-R--00-01684-408--SE, 2000.

[11] T. Wilkinson, “Applications of Ferroelectric Liquid Crystal LCOS Devices”, Ferroelectric liquid crystal conference, Oral presentation, Washington DC, August, 2001.

[12] K. D’havé, P. Rudquist, M. Matuszczyk, S.T. Lagerwall, H. Pauwels and R.S. Dabrowski, “Antiferroelectric liquid crystals with 45° tilt: new electro-opticeffects in liquid crystals”, *Proc. SPIE*, vol. 3955, pp. 33-44, 2000.

[13] K. D'havé, A. Dahlgren, P. Rudquist, J.P.F. Lagerwall, G. Andersson, M. Matuszczyk, S.T. Lagerwall, R.S. Dabrowski and W. Drzewinski, *Ferroelectrics*, vol. 244, pp. 115-128, 2000.

[14] D. S. Chemla, "Quantum Wells for Photonics", in selected papers on Fundamentals of Optoelectronics, SPIE milestone series; Vol. MS 90, Edited by Gordon R. Little, SPIE, Bellingham,Washington, pp. 195-202, 1994.

[15] R. C. Greenhow, *Introductory Quantum Mechanics*, Institute of Physics, London, 1990.

[16] R.B. Welstand , S.A. Pappert and P. K. L. Yu, "Electroabsorption", Wiley Encyclopedia of Electrical and Electronics Engineering Online, Webster J., Editor, John Wiley & Sons Inc., 1999.

[17] D. A. B. Miller et al, "Bandedge electro-absorption in quantum well structures: the quantum confined Stark effect", *J. Appl. Phys.*, vol. 53, 2173-2177, 1984 .

[18] T. L. Worchesky et al, "Large arrays of spatial light modulators hybridized to silicon integrated circuits", *Appl. Optics*, vol. 35, pp. 1180-1185, 1996.

[19] M. Whitehead, G. Parry and P. Wheatley, "Investigation of etalon effects in GaAs-AlGaAs multiple quantum well modulators", *IEE Proc*., vol. 136, no. 1, 1989.

[20] S. B. Alexander, *Optical Communication Receiver Design*, IEE Telecommunication Series, vol. 37, Michael Faraday House, Herts, 1997.

[21] E. Hällstig, M. Lindgren and L. Sjöqvist, "Study of a zero-twist nematic 128x128 SLM, FOI Report, FOI-R--0000--SE, 2001.

[22] "Electro-Optics Handbook", *TP-135*, Burle Industries Inc., 1974.

[23] O. Steinvall, "Theory for laser systems performance modelling", FOA Report, ISSN 1104-9154, FOA-R--97-00599-612--SE, 1997.

[24] M. Scheinfeld, N. S. Kopeika and R. Melamed, "Acquisition system for microsatellites laser communication in space", *Proc. SPIE*, vol. 3932, pp. 166-175, 2000.

[25] A. Berk, L. S. Bernstein and D. C. Robertson, "MODTRAN: a moderate resolution model for LOWTRAN7", Report No. GL-TR-89-0122, Geophysics Laboratory, Air Force Systems Command, Hanscom AFB, MA, 1989.

[26] Electro-Optical Systems Atmospheric Effects Library-EOSAEL, *LZTRAN- Laser transmittance module*, Ontar Corp., 1998, http://www.eosael.com.

[27] L. C. Andrews and R. L. Phillips, *Laser Beam Propagation through Random Media*, SPIE Press, Bellingham, Washington, 1998.

[28] L. C. Andrew and W. B. Miller, "Single-pass and double-pass propagation through complex paraxial optical systems", *J. Opt. Soc. Am. A*, vol. 12, pp. 137-150, 1995.

[29] J. H. Churnside and J. Wilson, "Enhanced backscatter of a reflected beam in atmospheric turbulence", *Appl. Opt*., vol. 32, pp. 2651-2655, 1993.

[30] GLAD 4.6 Theoretical Description" and "GLAD 4.6 Commands Descriptions" Manuals, Applied Optics Research, 1999, http://www.aor.com.

[31] J. W. Goodman, *Fourier Optics*, McGraw-Hill, 2nd ed., New York, 1996.

[32] L. Sjöqvist, “Laser countermeasures. GLAD simulations and evaluation of laser damage models”, FOA Report, FOA-R--99-01006-612--SE, 1999.

[33] C.J. Olsson,, H.W. Mocker, N.A. Demma och J.B. Ross, ”Coherent CO2 laser communication system with moduble retroreflectors”, *Appl. Optics*, vol. 39, pp. 2033-2043, 1995.

[34] P. B. Chu, N. R. Lo, E. C. Berg och K. S. J. Pister, ”Optical communication using micro corner cube reflectors”, 10th IEEE Int. Workshop on MEMS, (1997)

[35] L. C. Andrews, R. L. Phillips and A. R. Weeks, “Rytov approximation of the irradiance covariance and variance of a retroreflected optical beam in atmospheric turbulence”, *J. Opt. Soc. Am. A*, vol. 14, pp. 1938-1948, 1997.

[36] L. C. Andrews, C. Y. Young and W. B. Miller, “Coherence properties of a reflected optical wave in atmospheric turbulence”, *J. Opt. Soc. Am. A*, vol. 13, pp. 851-861, 1996.

[37] L. C. Andrews, R. L. Phillips and W. B. Miller, “Mutual coherence function for a double-passage retroreflected optical wave in atmospheric turbulence”, *Appl. Optics*, vol. 36, pp. 698-708, 1997.

[38] L. C. Andrews, R. L. Phillips and P. T. Yu, “Optical scintillations and fade statistics for a satellite-communication system”, *Appl. Optics*, vol. 34, pp. 7742-7751, 1995.

[39] P. Beckmann, *Probability in Communication Engineering*, Harcourt, Brace and World Inc., N.Y., 1967.

[40] M. A. Al-Habash, L. C. Andrews and R. L. Philips, “Mean Fade Time of an Optical Communication Channel Under Moderate-To-Strong Turbulence”, *Proc. SPIE*, vol. 3927, pp. 240-248, 2000.

APPENDIX 1 LASER BEAM PROPAGATION I DOUBLE-PASSAGE PHENOMENA

Closed analytical expressions describing turbulence effects and laser beam propagation have been derived for several interesting double-passage phenomena[27],[28],[35],[36],[37]. This appendix contains some relevant expressions for the retroreflective free-space optical communication system. Firstly, expressions for laser beam propagation in vacuum are reviewed. Turbulence effects including contributions from enhanced backscatter and fading characteristics are also considered. These atmosperic phenomena may give rise to major performance degradation of a retroreflective free-space optical communication system.

A1.1 Propagation in vacuum

Studying laser beam propagation in vacuum for a double-passage problem the notation developed by Andrew and Phillips is used for the notation of beam parameters. The irradiance at the transceiver in absence of atmospheric attenuation and turbulence effects can be written as[27]

$$I(r, 2L) = \frac{2P}{\pi W^2\left(1 + \frac{\Omega_R}{\Lambda_1}\right)} \cdot e^{-\frac{2r^2}{W^2}} \tag{A1}$$

where P is the laser power, W the effective beam radius and L the distance between the retromodulator and the transceiver. The factor $\left(1 + \frac{\Omega_R}{\Lambda_1}\right)$ accounts for the area of the retromodulator limiting the reflected intensity. The Gaussian beam parameters are defined according to

$$\Theta_o = 1 - \frac{L}{F_o} \tag{A2}$$

$$\Lambda_o = \frac{2L}{kW_o^2}$$

$$\Theta_1 = \frac{\Theta_o}{\Theta_o^2 + \Lambda_o^2}$$

$$\Lambda_1 = \frac{\Lambda_o}{\Theta_o^2 + \Lambda_o^2}$$

$$\Omega_R = \frac{2L}{kW_R^2}$$

where k is the wave vector, W_o is the beam radius at the transmitter and W_R is the radius of the retroreflector. In this formalism the retroreflector can be approximated by a Gaussian reflector. The effective beam radius at the transceiver can be calculated using the following expression

$$W = W_o\left[\frac{(2-\Theta_1)^2+(\Lambda_1+\Omega_R)^2}{\left(1+\frac{\Omega_R}{\Lambda_1}\right)(\Theta_1^2+\Lambda_1^2)}\right]^{\frac{1}{2}} \tag{A3}$$

The single- and double-pass propagation problems in complex paraxial systems have been discussed in detail by Andrew and Miller[28]. The (target) Fresnel ratio is commonly used to characterise the size of the retromodulator

$$\Omega_R = \frac{2L}{kW_R^2} \ . \tag{A4}$$

If the beam radius at the retromodulator, W_1, is considerably larger than the radius of the retromodulator then the reflector can be approximated to be a point target.

A1.2 Turbulence effects

As mentioned previously the most dominant turbulence effects are described in terms of

- transversal intensity variations (scintillations)
- beam spreading
- beam wandering
- angle-of-arrival fluctuations
- enhanced backscatter effects (double-passage phenomena).

In this paragraph theoretical expression which can be used to estimate how these phenomena affect the performance of a retroreflective free-space optical communication system are presented. The emphasis is focused on enhanced backscatter, scintillation and beam wandering. Beam spreading causes a decrease of the peak on-axis intensity reducing the range of the communication system.

The spatial frequency variation describing weak turbulence follow Kolmogorov statistics according to

$$\Phi_o(\kappa) = 0.033C_n^2\kappa^{-\frac{11}{3}} \tag{A5}$$

where κ is the spatial frequency and C_n^2 the structure parameter. The structure parameter describes the strength of the turbulence and varies between $C_n^2 = 10^{-16}$-$10^{-13}\mathrm{m}^{-2/3}$ in weak and medium turbulence cases, respectively. The structure parameter depends on the height relative ground, and studies of C_n^2 variations along slant paths suggest that up- and down-link cases should to be treated separately. In the discussion presented in this report horisontal path is considered i.e. C_n^2 is constant. However, several models exist which take the height dependence of C_n^2 into account. These models can be used in more advanced studies including effects of a varying structure parameter.

Studying the contribution from turbulence with respect to the on-axis intensity enhanced backscatter effect needs to be considered. The mean irradiance for a double-passage situation can be written as

$$\langle I(r, 2L)\rangle = \frac{I_o W_o^2}{W_e^2\left(1 + \frac{\Omega_R}{\Lambda_1}\right)} \cdot e^{-\frac{2r^2}{W_e^2}} N(r) \tag{A6}$$

where the effective beam radius is defined according to

$$W_e^2 = W^2(1 + T_i + T_R) \tag{A7}$$

T_i and T_r were defined by Andrew and Phillips and can be evaluated numerically for a given turbulence spectrum. T_i and T_R can be calculated as

(A8)

$$T_i = 4\pi^2 k^2 L \int_0^1 \int_0^\infty \kappa \Phi_n(\kappa) \left\{ 1 - \left(e^{-\frac{\Lambda_1 L \kappa^2}{k} \xi(\Theta_2 + \tilde{\Theta}_2 \xi + \Theta\xi)} \cdot e^{-\frac{L\kappa^2}{k}(1 - \tilde{\Theta}_1 \xi)(\Lambda_2 + -\Lambda_2 \xi + \Lambda\xi)} \right) \right\} d\kappa d\xi$$

and

$$T_R = 4\pi^2 k^2 L \int_0^1 \int_0^\infty \kappa \Phi_n(\kappa) \left\{ 1 - e^{-\frac{\Lambda_2 L \kappa^2 \xi^2}{k}} \right\} d\kappa d\xi \quad . \tag{A9}$$

$\tilde{\Theta}_1$ and $\tilde{\Theta}_2$ are defined in Appendix 2. The Kolmogorov spectrum, defined in eq. (5), was assumed to be valid for horisontal propagation paths assuming weak turbulence. The expressions presented above may also be utilised implementing alternative statistical turbulence characteristics. In the performance calculations the integrals in the expressions (8) and (9) were deduced numerically. The enhanced backscatter contribution can be estimated using the following
expression

$$N(r) = e^{B_I^{iR}(r, L)} \tag{A10}$$

The correlation contribution $e^{B_I^{iR}(r, L)}$ is derived for different target characteristics e.g. point target or extended target. Moreover, different expressions are obtained for plane, spherical and Gaussian waves[35],[36],[37].

The statistical effects of the fading due to scintillations and beam wander affect the bit error rate of the optical link. The statistics for the irradiance for a Gaussian beam can be described by the lognormal distribution according to[38]

$$p(I) = \frac{1}{I\sigma_I(r, 2L)\sqrt{2\pi}} \cdot e^{-\frac{\left[\ln\left(\frac{I}{\langle I(r, 2L)\rangle}\right) + \frac{1}{2}\sigma_I^2(r, 2L)\right]^2}{2\sigma_I^2(r, 2L)}} \tag{A11}$$

where $\sigma_I^2(r, 2L)$ defines the scintillation index. The scintillation index can be calculated for a double-passage configuration. The log-normal distribution in eq. (A11) is valid under the assumption of weak turbulence conditions. The mean irradiance for a double-passage communication channel is defined in eq. (A6). If we insert (A6) into (A11) and integrate to the fading threshold the following expression for the fractional fade time is obtained

$$P(I \le I_t) = \int_0^{I_t} \frac{1}{I\sigma_I(r, 2L)\sqrt{2\pi}} e^{-\frac{\left[\ln\left(\frac{I}{\langle I(0, 2L)\rangle}\right) + \frac{2r^2}{W_E^2} - B_I^{iR}(r, 2L) + \frac{1}{2}\sigma_I^2(r, 2L)\right]^2}{2\sigma_I^2(r, 2L)}} dI \, . \tag{A12}$$

The normalised on-axis irradiance is given as

$$\langle I(0, 2L)\rangle = \frac{W_o^2}{W_e^2\left(1 + \frac{\Omega_R}{\Lambda_1}\right)} . \tag{A13}$$

Expressions for calculating the scintillation index have been derived for plane, spherical and Gaussion waves in different type of target situations[27],[37]. The scintillation index can be derived from the covariance function available through the fourth order coherence function. If we integrate eq. (A12) the following expression describing the probability to obtain a level below the detection threshold

(A14)

$$P(I \le I_t) = \frac{1}{2}\left\{1 + erf\left[\frac{\ln\left(\frac{I_t}{\langle I(0, 2L)\rangle}\right) + B_I^{iR}(r, 2L) + \frac{1}{2}\sigma_I^2(0, 2L)}{\sqrt{2}\sigma_I(0, 2L)}\right]\right\}$$

The fractional fade time is the part of time the irradiance is below a given threshold value I_t. The fade level is usually defined according to

$$F_t = 10\log\left(\frac{\langle I(0, 2L)\rangle}{I_t}\right) \tag{A15}$$

The expression derived in (A14) can be employed to calculate the probability to be below the detection threshold (fractional fade time) as a function of the fade level, F_t. It should be noted that only on-axis situations are considered in the discussion above. Since the enhanced backscatter and the scintillation terms are calculated numerically off-axis effects can also be studied by a modification of eq. (A14).

Following the procedure by Andrews and coworkers the expected number of fades per unit time can be derived as (generalised to a double-passage situation)[38],[39]

$$\langle n(I_t)\rangle = \nu_o \cdot e^{-\left[\frac{\frac{1}{2}\sigma_I^2(0,2L) + \frac{2r^2}{W_E^2} + B_I^{iR}(0,2L) + \ln\left\{\frac{\langle I(0,2L)\rangle}{I_t}\right\}}{2\sigma_I^2(0,2L)}\right]} \tag{A16}$$

ν_o denotes the mean frequency and is defined via the covariance function of the irradiance[40]. The mean duration of fade time defining the mean time below a given intensity threshold value I_t can be derived

$$\langle t(I_t)\rangle = \frac{P(I < I_t)}{\langle n(I_t)\rangle} \tag{A17}$$

Using eqs. (A14) and (A16) the mean duration of a fade event can be estimated. The mean fade-time of an optical communication link has been studied under the assumption of moderate or strong turbulence conditions[40]. For moderate to strong turbulence situations the gamma-gamma probability distribution function was recently suggested to show more realistic behaviour for the mean fade time and the mean number of fades per unit time. Hence, it should be of interest to compare the results using the gamma-gamma and log-normal probability distribution functions in a double-passage situation resembling a retroreflective free-space optical communication system.

APPENDIX 2 NOMENCLATURE

Table 1 Nomenclature used in the formulas describing double-passage and turbulence effects.

Symbol	Parameter	Unit
W_o	Beam radius at transmitter	m
W_R	Effective radius retromodulator	m
W_1	Beam radius at retromodulator	m
W	Beam radius in receiver plane	m
I	Beam intensity	W/m^2
I_o	On-axis peak intensity	W/m^2
P_o, P_t	Laser power at transmitter	W
P_2, P_r	Captured power by the transceiver	W
L	Distance transmitter-retromodulator	m
F_o	Phase radius at transmitter	m
F_1	Phase radius at retromodulator	m
F	Phase radius at receiver	m
Θ_2	$\Theta_2 = 1 + \frac{L}{F}$	
Λ_2	$\Lambda_2 = \frac{2L}{kW^2}$	
$\tilde{\Theta}_1$	$\tilde{\Theta}_1 = 1 - \Theta_1$	
$\tilde{\Theta}_2$	$\tilde{\Theta}_2 = 1 - \Theta_2$	
A_Δ	Retromodulator cross-section	m^2
A_t	Effective area of the optical receiver aperture	m^2
η_r	Optical losses in the transmitter	
η_t	Optical losses in the retromodulator	
η_{atm}	Optical attenuation due to scattering	
θ_t	Divergence laser transmitter beam	rad
θ_r	Divergence of reflected beam - retromodulator	rad